

Exploring the History of Stellar Mergers with Chemistry: Examining the Origins of Massive α -Enriched Stars using Carbon Isotope Ratios

ZACHARY G. MAAS,¹ KEITH HAWKINS,² JEFFREY M. GERBER,³ ZOE HACKSHAW,² AND CATHERINE MANEA⁴

¹*Indiana University, Astronomy Department, 727 East Third Street, Bloomington, IN 47405, USA*

²*Astronomy Dept., The University of Texas at Austin, 2515 Speedway Boulevard, Austin, TX 78712, USA*

³*Purdue University, Department of Physics and Astronomy 525 Northwestern Ave West Lafayette, IN 47907, USA*

⁴*Columbia Astrophysics Laboratory, Columbia University, New York, NY, 10027, USA*

ABSTRACT

Recently discovered massive α -enriched (MAE) stars have surface chemistry consistent with members of the older thick disk Milky Way population but high masses ($\sim 1.5 - 3 M_{\odot}$) that suggest these stars are young. The origin of MAE stars is not fully understood although binary interactions are likely an important formation pathway. To better constrain the history of MAE stars, we have measured metallicities, carbon isotope ratios, and CNO abundances in 49 red clump stars and four red giants. Our sample included thin disk, thick disk, and MAE stars to best constrain different formation scenarios. We observed our sample stars using the Tull spectrograph on the McDonald 2.7m telescope and derived abundances using synthetic spectra created by the **Turbospectrum** radiative transfer code. Overall, we find that 10 of our red clump MAE stars are consistent with the average thick disk carbon isotope ratio of $^{12}\text{C}/^{13}\text{C} = 8.2 \pm 3.4$. We find five MAE stars that have significantly higher carbon isotope ratios ($^{12}\text{C}/^{13}\text{C} > 15$) than stars at similar metallicities. Two of the anomalous stars show abundance patterns consistent with AGB mass transfer while three MAE stars have $^{12}\text{C}/^{13}\text{C}$ ratios similar to massive, single RC stars and show no clear signs of binarity from radial velocity monitoring or from the Gaia RUWE measurement. Overall, we find that carbon isotope ratio measurements provide a unique constraint when discerning the possible origins of MAE stars.

Keywords: *Stellar abundances (1577) — Red giant clump (1370) — Galaxy stellar content (621)*

1. INTRODUCTION

Industrial scale chemical evolution surveys have revealed new stellar populations in the Milky Way. The information from asteroseismology and spectroscopic abundances has discovered stars with high masses ($\sim 1.5 - 3 M_{\odot}$) and high $[\alpha/\text{Fe}]$ ratios (M. Martig et al. 2015; C. Chiappini et al. 2015). The relatively high masses imply these stars are young while the high $[\alpha/\text{Fe}]$ ratios are consistent with the chemical composition of stars in the Milky Way thick disk. Multiple formation pathways have been proposed for these objects. One possibility is that MAE stars¹ may be born from gas with less Type Ia SN contributions and then are displaced outward by the bar. Another scenario suggests that MAE stars were

older objects with enhanced masses due to stellar mergers or mass transfer (M. Martig et al. 2015; C. Chiappini et al. 2015). High-resolution optical follow-up of MAE stars have corroborated the α -enhancement and found radial velocity variations consistent with a binary system (P. Jofré et al. 2016; D. Yong et al. 2016; T. Matsuno et al. 2018). Additional long-term study of MAE stars have also found a significant fraction of their sample appear as binary stars while some MAE stars show no radial velocity variation (P. Jofré et al. 2023).

Another potential method to exploring the origins of MAE stars is to examine elements altered through internal mixing processes during stellar evolution. Proton-capture (p-capture) burning cycles are strongly temperature-dependent and therefore will correlate to mass. As the star evolves along the sub-giant and red giant branch, the p-capture burning products created in the CNO cycle are transported from the core to the surface, and specific elements may be used as a diagnostic of nucleosynthesis occurring in the interior

Email: zmaas@iu.edu

¹ We refer to these objects as massive α -enriched stars instead of α -rich young stars since the stellar ages are inferred from masses which may have changed over time due to mass-transfer events or stellar mergers.

of the star (J. Iben 1967). Ratios of ^{12}C , ^{13}C , and N are especially sensitive to mass, metallicity, and evolutionary state. Models of disk evolution predict a large fraction of mergers of low-mass stars occur after the first dredge-up and therefore their C and N abundances are expected to be consistent with low mass stars (R. G. Izzard et al. 2018). Follow-up measurements of CNO abundances in 51 MAE stars found that some stars had [C/N] ratios that reflected low-mass stars after the first dredge up while other were consistent with higher mass stars (P. Jofré et al. 2016; S. Hekker & J. A. Johnson 2019; W. X. Sun et al. 2020; M. Zhang et al. 2021). The [C/N] ratio is mass-sensitive for red-giant stars and the wide range of [C/N] found in MAE stars suggests multiple pathways of binary star evolution necessary to produce a MAE star (P. Jofré et al. 2016; S. Hekker & J. A. Johnson 2019; W. X. Sun et al. 2020; M. Zhang et al. 2021).

A statistical analysis of MAE stars identified from the LAMOST survey demonstrated that MAE stars had similar kinematics and [C/N] ratios as thick disk stars (Y. Huang et al. 2020; W. X. Sun et al. 2020). Beyond [C/N] and kinematics, some MAE stars have been found to be s-process enhanced in elements like Ce and Ba, elements primarily synthesized in asymptotic giant branch stars (M. Zhang et al. 2021; V. Cerqui et al. 2023). Multiple binary interaction scenarios have been discussed in the literature and the possible components include combinations of main-sequence, red giant branch stars, and asymptotic giant branch stars that can completely merge, have a common envelop phase, or undergo mass-transfer (P. Jofré et al. 2016; M. Zhang et al. 2021; V. Cerqui et al. 2023). Similar pathways have been necessary when discerning the history of possible field blue straggler stars.

One potentially important way to distinguish the formation scenarios of evolved MAE stars is through measurements of the $^{12}\text{C}/^{13}\text{C}$ ratio. Since the CNO-process directly increases the ^{13}C abundance in a star’s interior, stellar mixing changes the surface abundance beginning with the first dredge-up on the sub giant branch when ^{13}C rich material is brought from the interior to the surface (J. Iben 1965; C. Charbonnel 1995). The mixing efficiency varies depending on metallicity; red giant branch metal rich disk stars have been observed to have carbon isotope ratios of 20-40, while the decrease is even more drastic for metal poor stars (A. I. Boothroyd & I. J. Sackmann 1999) (as a reference main-sequence solar-twins span $70.9 < ^{12}\text{C}/^{13}\text{C} < 103.4$, R. B. Botelho et al. 2020).

Non-canonical extra-mixing occurs for low-mass stars between $0.5 M_{\odot} \lesssim M_{\text{star}} \lesssim 2.0 M_{\odot}$ after the star passes

the luminosity function (LF) bump on the red giant branch. The extra-mixing further lowers the carbon isotope ratios as additional CNO-cycle material is dredged up from the H-burning shell around the core to the photosphere. Multiple theoretical models have been proposed to explain the extra-mixing, such as thermohaline mixing (R. Kippenhahn et al. 1980; C. Charbonnel & J. P. Zahn 2007; P. P. Eggleton et al. 2008; M. Cantiello & N. Langer 2010; F. C. Wachlin et al. 2011; N. Lagarde et al. 2012), rotation-induced mixing (A. V. Sweigart & J. G. Mengel 1979; J. Chanamé et al. 2005; A. Palacios et al. 2006), magnetic mixing mechanisms (M. Busso et al. 2007; J. Nordhaus et al. 2008; S. Palmerini et al. 2009), and internal gravity waves (P. A. Denissenkov & C. A. Tout 2000). Observational evidence of extra-mixing has been identified in the CNO abundances of field giants and clusters. Specifically, low $^{12}\text{C}/^{13}\text{C}$ ratios have been observed in field stars (R. G. Gratton et al. 2000; L. D. Keller et al. 2001; M. Spite et al. 2006; G. Tautvaišienė et al. 2013; C. Aguilera-Gómez et al. 2023), open clusters (R. Smiljanic et al. 2009; G. Tautvaišienė et al. 2016; L. Szigeti et al. 2018; C. McCormick et al. 2023), and in globular clusters (N. B. Suntzeff & V. V. Smith 1991; M. M. Briley et al. 1997; M. D. Shetrone 2003; G. H. Smith et al. 2007; A. Recio-Blanco & P. de Laverny 2007; Z. G. Maas et al. 2019).

The summary of these observations and models demonstrates that the extra-mixing processes are dependent on stellar mass and metallicity. For the $^{12}\text{C}/^{13}\text{C}$ ratio specifically, more metal-poor stars dredge up more ^{13}C and low-mass stars dredge up more ^{13}C as predicted by thermohaline mixing models (e.g. C. Charbonnel & N. Lagarde 2010; N. Lagarde et al. 2012) and from observations of stars (e.g. G. Tautvaišienė et al. 2016; C. Aguilera-Gómez et al. 2023). Specifically, higher mass core He-burning stars are expected to have $^{12}\text{C}/^{13}\text{C}$ ratios of ~ 20 , while lower mass core He-burning stars have $^{12}\text{C}/^{13}\text{C}$ ratios of ~ 10 (C. Charbonnel & N. Lagarde 2010; N. Lagarde et al. 2012).

One intriguing avenue to study MAE stars is by measuring the $^{12}\text{C}/^{13}\text{C}$ ratio and comparing to disk stars at similar metallicities. The types and timing of mass transfer and/or merger events may be constrained by this photospheric abundance since there are clear points in stellar evolution where the $^{12}\text{C}/^{13}\text{C}$ ratio changes. To this end, we have measured the $^{12}\text{C}/^{13}\text{C}$ in multiple thin disk, thick disk, and MAE stars. The observations and sample selection are described in section 2. The abundance measurement methodology is detailed in section 3 with a description of the measurement uncertainty in section 4. The discussion of the results is found in section 5. Finally, the results are described in 6.

2. SAMPLE SELECTION AND OBSERVATIONS

2.1. *Selecting Stars in Different Stellar Populations*

In order to detect differences in the composition of MAES stars and typical field giants, we require a selection of stars at similar evolutionary states to minimize systematic differences due to stellar mixing, a sample of stars at different masses, and finally, stars that are bright enough to achieve the required signal-to-noise ratios (S/N) to detect weak molecular absorption lines. Our sample has been selected from the Y. Huang et al. (2020) catalog of $\sim 140,000$ red clump (RC) stars. The RC stars were identified using data from the Large Sky Area Multi-Object Fibre Spectroscopic Telescope (LAMOST) survey and the methodology of Y. Huang et al. (2015). Masses and ages were derived for the RC sample using a KPCA (B. Schölkopf et al. 1998) machine-learning analysis. The test and training samples were created from a crossmatch of 4185 stars with measured asteroseismic masses and ages from J. Yu et al. (2018). The principle component analysis was applied to the LAMOST blue-arm spectrum for each object, which spanned from 3900 Å to 5500 Å. No systematic discrepancies between age and mass residuals with atmospheric parameters were detected (Y. Huang et al. 2020). Stellar population mass distributions from W. X. Sun et al. (2020) are similar to RGB stars from (M. Zhang et al. 2021). We note that some low-mass ($< 1.3 M_{\odot}$) MAE stars exist in our sample and are slightly offset compared to asteroseismic MAE star samples (e.g. M. Martig et al. 2015) but within the typical errors for mass measurements ($\pm 0.2 M_{\odot}$).

The mass measurement methodology follows previous KPCA analysis of LAMOST spectra (M. S. Xiang et al. 2017; Y. Wu et al. 2018, 2019) and was validated using observations of open cluster members. A combination of spectral features sensitive to atmospheric parameters, $[\alpha/\text{Fe}]$, and CN abundances all are potentially used in the KPCA analysis. W. X. Sun et al. (2020) states that all features, not just CN, were used when determining masses and Y. Wu et al. (2018) shows that ages from only [C/N] ratios for red giant branch stars are correlated, but not identical, to ages from KPCA analysis.

We selected thin disk, thick disk, and MAES stars from this RC catalog for observations. Selection criteria was adopted from W. X. Sun et al. (2020) and included:

- Quality Cuts: Age < 14 Gyr, Age error less than 50%, $[\text{Fe}/\text{H}] > -1$ dex, 10 % distance errors, and Gaia DR3 Gmag < 12 mag
- Thin Disk: $0 < \text{Age} < 6$ Gyr, $[\alpha/\text{Fe}] < 0.1$ dex
- Thick Disk: $8 < \text{Age} < 14$ Gyr, $[\alpha/\text{Fe}] > 0.2$ dex

- MAES: $0 < \text{Age} < 6$ Gyr, $[\alpha/\text{Fe}] > 0.2$ dex

We added the G-band magnitude restriction from Gaia DR3 data (Gaia Collaboration et al. 2023) to ensure we can achieve our S/N target of ~ 100 at 8000 Å (the wavelength region near the CN feature from which we determine $^{12}\text{C}/^{13}\text{C}$ ratios). The total RC sample that meets these criteria are plotted in Fig. 1 and are color-coded depending on stellar population membership given in Table 1.

We also wanted to remove any potential non-RC star contaminants drawn to ensure outlier stars do not impact our analysis of MAE star origins. We derived absolute G band magnitudes to see if our stars were photometrically consistent with RC stars using Gaia DR3 photometry (Gaia Collaboration et al. 2021, 2023), extinction corrections from dustmaps (v. 2019) (G. M. Green et al. 2019), and dust extinction conversions to Gaia filters from S. Wang & X. Chen (2019). The “bayestar2019” dust map option was used to determine the extinction for each star. The distances were adopted from the C. A. L. Bailer-Jones et al. (2021) catalog to calculate the absolute G magnitude for each star in our sample. We plot our stars along with the targets with a subsample of Y. Huang et al. (2020) stars in Fig. 1. We also only use stars that meet the photometric criteria of: $0.0 < M_G < 0.9$ and $1.02 < \text{BP-RP} < 1.27$. We adopt these limits because redder stars are more likely to be red giants with high $^{12}\text{C}/^{13}\text{C}$ ratios, brighter stars may be beginning to ascend the AGB and start dredging up ^{12}C , and finally low-luminosity stars may be anomalous objects, such as pre-main sequence stars. All of our stars fall within or near the 84% percentile of stars with similar photometric properties to help remove outliers, as seen in Fig. 1.

We supplement our RC sample chosen from Y. Huang et al. (2020) with additional MAE stars that were identified from a combination of asteroseismology and chemical composition analysis. We separately identify the stars in our sample with asteroseismic masses as Kepler stars in plots and tables. Information about these targets is described in Table 2. The objects were identified by S. Hekker & J. A. Johnson (2019); P. Jofré et al. (2023), with masses originally derived from APOKASC (M. H. Pinsonneault et al. 2018).

2.2. *Observation Summary and Data Reduction*

Observations were obtained using the Tull Coudé spectrograph on the McDonald 2.7m telescope. We used the TS23 set-up with slit 4 to achieve a resolution of $R \sim 60,000$. The ^{13}CN feature at ~ 8005 Å was targeted and the CCD prism/grating settings were adjusted to ensure this feature was not off or at the edge of the CCD. We

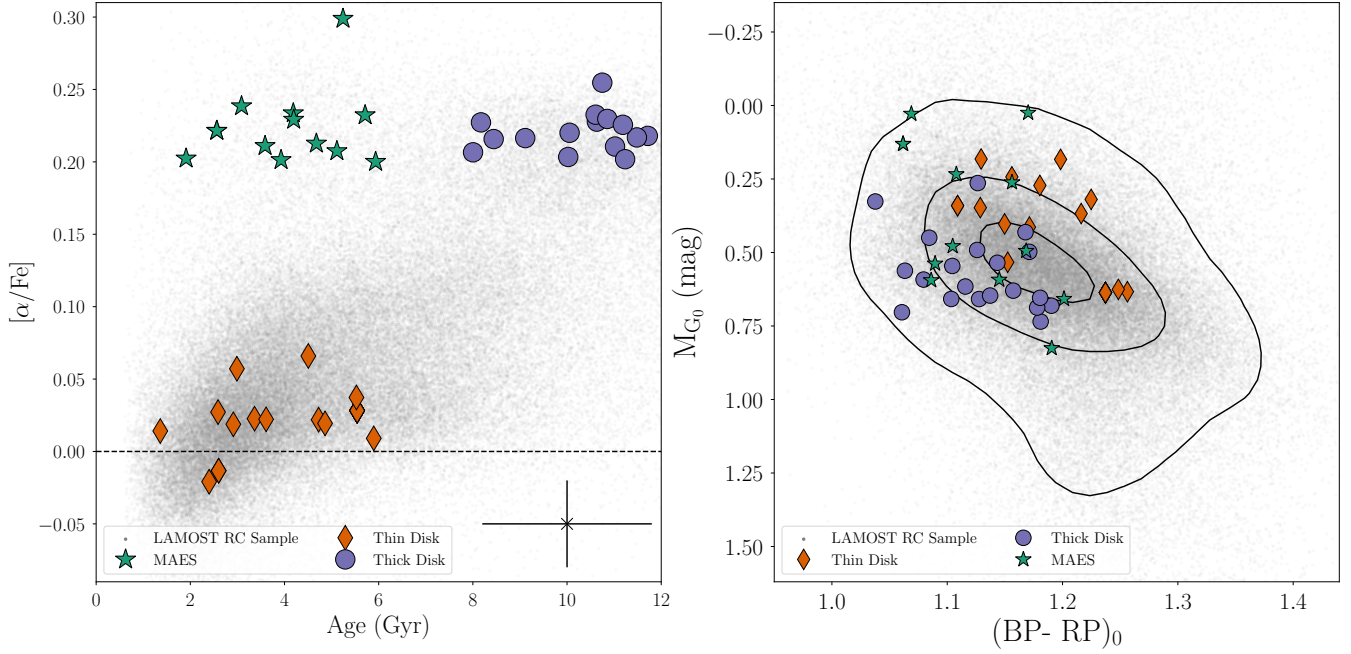


Figure 1. Left: The stars selected from *Y. Huang et al. (2020)* and analyzed in this work are represented as green stars for MAES stars, blue circles for thick disk stars, and orange diamonds for thin disk stars. Gray points are the rest of the LAMOST RC catalog that was unobserved. The figure shows ages compared to $[\alpha/\text{Fe}]$ enrichment with parameters from *Y. Huang et al. (2020)*. The mean age and $[\alpha/\text{Fe}]$ uncertainties for our sample stars is shown as a black x. Right: We show a color-magnitude diagram for our targets selected from *Y. Huang et al. (2020)*. Contours represent 16%, 50%, 84% density values for the total sample. The extinction correction methodology is described in subsection 2.1.

also observed RC stars from *M. Afşar et al. (2012)* to validate our methodology since these objects were previously analyzed using the same instrument/facility combination and have derived carbon isotope ratios using the same CN feature used in this work.

Data reduction was done using IRAF² (*D. Tody 1986, 1993*) with the PyRAF³ wrapper (*Science Software Branch at STScI 2012*). The science images were trimmed and bias corrected with *ccdproc*. Cosmic rays were removed using the *cosmicrays* task. Pixel-to-pixel variations were corrected with a quartz lamp flat-field image. The echelle spectra were corrected for scattered light using *apscatter* and extracted with *apall*.

The wavelength solution for the observations was determined with ThAr lamp observations for each night and the dispersion to the emission line location fits were typically 0.003 \AA . The reduced spectra were then normalized using a spline function and the separate apertures were combined. Telluric standards were observed

and the CN region was examined for potential contamination. The *telluric* task in IRAF was used to removed telluric lines for stars where the ^{13}CN line region when a blend was detected.

We used *iSpec* (*S. Blanco-Cuaresma et al. 2014; S. Blanco-Cuaresma 2019*) to measure and correct for the radial velocities of each star using a cross-correlation technique with a solar template spectrum. Typical radial velocity uncertainties from *iSpec* cross-correlation range for 0.1 km/s to 0.2 km/s . When compared to Gaia DR3 (*Gaia Collaboration et al. 2023*), our sample has an average radial velocity difference of $-0.04 \pm 2.46 \text{ km/s}$. There are four outlier stars with radial velocity differences beyond 5 km/s and when they are removed the average becomes $0.05 \pm 1.21 \text{ km/s}$. Finally, stars with multiple exposures were mean combined after the RV correction. Due to significant blending and low S/N ratios in the blue region of the spectrum, we restricted our analysis to $4700 \text{ \AA} - 8800 \text{ \AA}$ for abundance analysis. Observation dates and signal to noise ratios for our sample are listed in Table 1.

² IRAF is distributed by the National Optical Astronomy Observatory, which is operated by the Association of Universities for Research in Astronomy, Inc., under cooperative agreement with the National Science Foundation

³ PyRAF is a product of the Space Telescope Science Institute, which is operated by AURA for NASA.

Table 1. LAMOST RC Observation Log

Gaia DR3 ID	Date Obs. (UT Date)	S/N Ratio pixel ⁻¹ at 8000 Å	G (mag)	A _G (mag)	M _G (mag)	Age (Gyr)	σ Age (Gyr)	[α /Fe] (dex)	σ [α /Fe] (dex)	Pop.
1520951449701176832	2021-01-22	159	9.45	0.01	0.50	11.72	3.18	0.22	0.03	ThickDisk
3872367429179326592	2021-01-22	117	10.23	0.01	0.23	4.20	1.14	0.23	0.03	MAES
3283445774160853632	2021-01-23	117	10.30	0.71	0.54	12.34	3.35	0.21	0.03	ThickDisk
3876280792926214272	2021-01-23	108	10.67	0.13	0.59	3.59	0.98	0.21	0.03	MAES
723448831119162752	2021-01-23	147	9.90	0.01	0.66	11.02	2.99	0.21	0.03	ThickDisk
3222153253655970176	2021-01-23	120	10.08	0.15	0.55	13.07	3.54	0.21	0.03	ThickDisk
672933143771515392	2021-01-23	105	10.42	0.10	0.54	5.24	1.42	0.30	0.03	MAES
3813076676968705408	2021-01-23	208	9.92	0.01	0.63	12.69	3.44	0.22	0.03	ThickDisk
3878388801529524480	2021-02-21	93	10.63	0.02	0.13	2.56	0.70	0.22	0.03	MAES
4008867227922925824	2021-02-21	186	9.33	0.04	0.73	8.00	2.17	0.21	0.03	ThickDisk
607150428232731008	2021-02-21	123	9.50	0.16	0.66	5.11	1.39	0.21	0.03	MAES
3163974593033517824	2021-02-21	91	10.16	0.02	0.69	9.11	2.47	0.22	0.03	ThickDisk
971925848973504512	2021-02-21	119	9.68	0.56	0.03	4.19	1.15	0.23	0.03	MAES
1235499505072865792	2021-02-22	138	9.53	0.04	0.59	5.93	1.62	0.20	0.03	MAES
636614659798851712	2021-02-22	150	9.93	0.05	0.03	3.09	0.84	0.24	0.03	MAES
3882249324293741440	2021-02-22	133	10.39	0.07	0.49	10.61	2.88	0.23	0.03	ThickDisk
3326023296796724096	2021-02-22	78	9.39	0.10	0.63	5.90	1.60	0.01	0.03	ThinDisk
3130104824535988096	2021-02-22	153	10.16	0.29	0.59	10.75	2.91	0.25	0.03	ThickDisk
1486503509885506944	2021-04-25	106	8.86	0.02	0.24	4.51	1.22	0.07	0.03	ThinDisk
1330490025449104640	2021-04-25	96	9.44	0.12	0.53	4.86	1.32	0.02	0.03	ThinDisk
1312079562236150656	2021-04-25	91	9.25	0.04	0.41	2.59	0.71	0.03	0.03	ThinDisk
1388620891675799168	2021-04-25	127	7.46	0.02	0.40	2.91	0.79	0.02	0.03	ThinDisk
3833688568619253120	2021-04-27	81	8.83	0.02	0.63	3.61	0.99	0.02	0.03	ThinDisk
3976085529258764800	2022-03-11	78	9.27	0.04	0.64	5.54	1.50	0.03	0.03	ThinDisk
688166190179213184	2022-03-11	64	9.40	0.20	0.34	2.60	0.71	-0.01	0.03	ThinDisk
3811610203335180416	2022-03-12	123	9.80	0.05	0.70	10.05	2.73	0.22	0.03	ThickDisk
866507457241940480	2022-03-12	105	8.85	0.12	0.35	2.40	0.65	-0.02	0.03	ThinDisk
638939267896892800	2022-03-12	67	10.19	0.13	0.26	1.91	0.52	0.20	0.03	MAES
1156535637983109376	2022-03-12	157	9.89	0.09	0.68	10.03	2.72	0.20	0.03	ThickDisk
3952269007889690752	2022-03-12	104	9.92	0.05	0.45	8.44	2.29	0.22	0.03	ThickDisk
3976449776845278592	2022-03-13	99	9.11	0.05	0.18	2.99	0.81	0.06	0.03	ThinDisk
685849244302001408	2022-03-13	166	10.21	0.09	0.48	5.71	1.55	0.23	0.03	MAES
1447162502806921472	2022-03-13	111	9.44	0.04	0.37	5.53	1.50	0.04	0.03	ThinDisk
1457380298724918528	2022-03-13	164	10.02	0.03	0.56	8.17	2.22	0.23	0.03	ThickDisk
4009353280781776384	2022-03-13	152	9.24	0.05	0.18	3.36	0.91	0.02	0.03	ThinDisk
1170340693664424192	2022-03-13	102	10.10	0.07	0.65	12.52	3.41	0.24	0.05	ThickDisk
3096606828405802240	2022-03-14	79	10.63	0.06	0.43	14.41	3.90	0.22	0.03	ThickDisk
1500728407210595200	2022-03-14	97	10.16	0.10	0.26	11.48	3.11	0.22	0.03	ThickDisk
4034411734894241024	2022-03-14	121	10.50	0.05	0.66	11.19	3.03	0.23	0.03	ThickDisk
842398878096774784	2022-03-14	108	8.76	0.03	0.32	4.72	1.29	0.02	0.03	ThinDisk
579491624824868608	2022-03-14	121	10.46	0.05	0.83	3.93	1.07	0.20	0.03	MAES
3138549726673657600	2022-03-15	95	9.39	0.02	0.27	1.36	0.38	0.01	0.03	ThinDisk
640282939825239936	2022-03-15	128	9.94	0.05	0.62	10.63	2.88	0.23	0.03	ThickDisk
3671355056986858880	2022-03-15	70	10.75	0.09	0.49	4.68	1.27	0.21	0.03	MAES
3869545635666293504	2022-03-15	150	10.69	0.06	0.65	11.23	3.05	0.20	0.03	ThickDisk
3973325544619220224	2022-03-15	131	10.17	0.34	0.33	10.85	2.94	0.23	0.03	ThickDisk

G-band magnitudes are from Gaia eDR3 [Gaia Collaboration et al. \(2021\)](#), ages and [α /Fe] are from [Y. Huang et al. \(2020\)](#). The "Pop." column refers to the assigned stellar population and includes: TD = Thin Disk, ThD = Thick Disk, and MAES = Massive α -Enhanced Star.

Table 2. Kepler MAES Observation Log

Kepler ID	Date Obs. (UT Date)	S/N Ratio pixel ⁻¹ at 8000 Å	G (mag)	Spectral Type
KIC 8539201	2021-04-25	123	9.45	RC
KIC 3833399	2022-03-12	93	9.45	RC
KIC 5687374	2023-07-11	125	10.42	RG
KIC 5966873	2023-07-11	85	9.75	RG
KIC 3455760	2023-07-12	89	10.9	RG
KIC 10525475	2023-07-12	87	10.73	RC
KIC 4149831	2023-07-13	90	10.49	RC

G-band magnitudes of Kepler stars in our sample are from Gaia DR3 [Gaia Collaboration et al. \(2023\)](#). RC = Red clump and RG = Red giant for spectral type.

3. ABUNDANCE MEASUREMENT METHODOLOGY

3.1. Atmospheric Parameter Measurements with BACCHUS

Our primary goal is to measure precise carbon isotope ratios for our sample of stars using a ¹³CN absorption line at 8005 Å. We require the full CNO abundances, since the molecular equilibrium and therefore CN molecular feature line strengths, depend on the chemical composition of the star. Our measurements were performed using *turbospectrum* (B. Plez 2012; J. M. Gerber et al. 2023), MARCS model atmospheres (B. Gustafsson et al. 2008), and the Gaia-ESO Survey linelist (U. Heiter et al. 2021) which uses CN line data from J. S. A. Brooke et al. (2014). All abundances reported are scaled to the solar abundances of E. Magg et al. (2022).

We derived atmospheric parameters using the Brussels Automatic Code for Characterizing High accuracy Spectra (BACCHUS) (T. Masseron et al. 2016a). The BACCHUS pipeline (T. Masseron et al. 2016b) was utilized to measure equivalent widths of Fe I and Fe II lines and iteratively measured atmospheric parameters through iron excitation-ionization balance. BACCHUS outputs include the effective temperature, surface gravity, [Fe/H], microturbulence, and convolution parameter used to smooth the spectra to compensate for the instrument profile, stellar broadening mechanisms, etc. We additionally measured C and Mg abundances with BACCHUS by analyzing atomic C I lines (near ~ 5,000 Å) and Mg I features. The final atmospheric parameters are listed in Table 3.

3.2. ¹³C, N, and O Abundances with *TSFitPy*

Oxygen abundance measurements were more complicated as the the 6300 Å feature fell into a order gap in our observations and the 6363 Å line suffers from blends with CN lines and a Ca auto-ionization line (J. Mitchell & O. C. Mohler 1965; D. L. Lambert 1978). We derived

Table 3. Star Atmospheric Parameters

Gaia DR3 ID	Kepler ID	T_{eff} (K)	log(g) (dex)	[Fe/H] (dex)	ξ (kms ⁻¹)
1520951449701176832	-	4792	2.49	-0.45	1.48
3872367429179326592	-	4964	2.68	-0.58	1.46
3283445774160853632	-	4844	2.10	-0.74	1.52
3876280792926214272	-	4923	2.27	-0.50	1.34
723448831119162752	-	4933	2.62	-0.59	1.53
3222153253655970176	-	4952	2.59	-0.55	1.51
672933143771515392	-	4916	2.12	-0.87	1.62
3813076676968705408	-	4833	2.46	-0.49	1.44
3878388801529524480	-	5033	2.62	-0.75	1.39
4008867227922925824	-	4781	2.46	-0.39	1.56
607150428232731008	-	4546	2.30	-0.51	1.25
3163974593033517824	-	4839	2.27	-0.46	1.39
971925488973504512	-	4819	2.59	-0.74	1.35
1235499505072865792	-	4796	2.25	-0.44	1.38
636614659798851712	-	4985	2.44	-0.60	1.35
3882249324293741440	-	4848	2.48	-0.58	1.56
3326023296796724096	-	4695	3.07	0.24	1.35
3130104824535988096	-	4868	2.62	-0.49	1.43
1486503509885506944	-	4779	2.44	-0.34	1.24
1330490025449104640	-	4742	2.58	-0.12	1.32
1312079562236150656	-	4784	2.57	-0.03	1.26
1388620891675799168	-	4857	2.80	-0.16	1.34
3833688568619253120	-	4616	2.69	0.14	1.27
3976085529258764800	-	4708	2.77	0.07	1.36
688166190179213184	-	4644	2.77	0.11	1.30
3811610203335180416	-	5128	2.58	-0.64	1.64
866507457241940480	-	4773	2.72	-0.02	1.28
638939267896892800	-	4980	2.93	-0.38	1.57
1156535637983109376	-	4744	2.53	-0.37	1.36
3952269007889690752	-	4960	2.62	-0.62	1.53
3976449776845278592	-	4716	2.46	-0.09	1.46
685849244302001408	-	4938	2.73	-0.49	1.46
1447162502806921472	-	4656	2.27	-0.14	1.39
1457380298724918528	-	4983	2.51	-0.70	1.37
4009353280781776384	-	4852	2.70	-0.11	1.51
1170340693664424192	-	4756	2.55	-0.37	1.40
3096606828405802240	-	4792	2.65	-0.41	1.43
1500728407210595200	-	4773	2.50	-0.53	1.51
4034411734894241024	-	4741	2.67	-0.30	1.40
842398878096774784	-	4674	2.44	-0.05	1.28
579491624824868608	-	4824	3.00	-0.27	1.43
3138549726673657600	-	4837	2.83	0.03	1.32
640282939825239936	-	4879	2.58	-0.56	1.49
3671355056986858880	-	4690	2.78	-0.32	1.21
3869545635666293504	-	4877	2.60	-0.43	1.52
3973325544619220224	-	4807	2.33	-0.65	1.60
2117411734401094528	KIC 8539201	4929	2.37	-0.68	1.42
2100234510918046592	KIC 3833399	4572	2.33	-0.07	1.26
2077396108227657344	KIC3455760	4581	2.35	-0.16	1.19
2100961185027552384	KIC4149831	4642	1.92	-0.50	1.56
2103822354798961280	KIC5687374	4259	1.47	-0.57	1.44
2077396108227657344	KIC5966873	4532	1.96	-0.49	1.41
2130894220860474752	KIC10525475	4748	2.65	-0.23	1.52

Solar Abundance Scale from E. Magg et al. (2022)

oxygen abundances using the high-excitation triplet at ~ 7770 Å using `TSFitPy` (J. M. Gerber et al. 2023; N. Storm & M. Bergemann 2023). These lines are known to be significantly affected by Non-LTE effects (e.g. E. Magg et al. 2022) and the `TSFitPy` spectral modeling routine utilizes an NLTE version of `turbospectrum` (J. M. Gerber et al. 2023). The three O I lines were fit individually and the mean abundances are reported as the [O/H] abundances for each star.

The N abundances were determined using ^{12}CN lines near $\sim 8000 - 8050$ Å. The set of lines in the region were fit simultaneously using the `TSFitPy` routine, and the abundance that best minimized the χ^2 was adopted as the final [N/Fe] abundance. Once all CNO abundances were derived, grids of synthetic spectra near the ^{13}CN feature at 8005 Å were created using `TSFitPy` for each star in our sample. The $^{12}\text{C}/^{13}\text{C}$ ratios were varied by 1 in each grid, spanning from $2 < ^{12}\text{C}/^{13}\text{C} < 50$. The features were fit to each observed spectrum and the model that minimized the χ^2 was adopted as the final $^{12}\text{C}/^{13}\text{C}$ ratio.

4. ABUNDANCE UNCERTAINTY AND LITERATURE COMPARISONS

4.1. Comparison to Afşar et al. 2012

We observed RC abundance standard stars from M. Afşar et al. (2012) over multiple nights to examine the accuracy and precision of our atmospheric parameters and chemical abundances. Abundance standards were chosen from M. Afşar et al. (2012) since that analysis also used the Tull Spectrograph on the McDonald 2.7m telescope, at a similar resolution, and derived ^{13}C , N, and O abundances. A log of the observations, our derived parameters, and the literature abundances are listed in Table 4.

Atmospheric parameters in M. Afşar et al. (2012) were derived using iron excitation abundance analysis, similar to the BACCHUS analysis in this work, with estimated uncertainties on the effective temperature of ± 150 K, the $\log(g)$ value of ± 0.3 dex, and an uncertainty of $0.1 - 0.2$ dex for [Fe/H]. M. Afşar et al. (2012) also derived solar abundances using a high-resolution solar atlas. Solar abundances were measured for different atomic and molecular lines; for example the neutral C I solar abundance was $A(\text{C}) = 8.53$, while the CH molecule provided a $A(\text{C}) = 8.38$. Since the solar scale appears to remove systematic effects in the abundance analysis we did not re-normalize the M. Afşar et al. (2012) abundances. Additionally, the common elements between both M. Afşar et al. (2012) and this study, such as the C I lines, have similar solar abundances as our adopted values from E. Magg et al. (2022).

We determined that our internal parameter consistency is on the order of 20-30 K for T_{eff} , $0.1 - 0.2$ for $\log(g)$, and $0.02-0.05$ dex for [Fe/H] from our repeated observations. The C and N abundances show limited star to star scatter, while the oxygen abundances have larger internal dispersion at 0.1 dex. The abundances derived in each repeated observation are consistent with one another, as shown in Table 4. When compared to M. Afşar et al. (2012), we find consistent T_{eff} but different $\log(g)$ values on the order of $0.1 - 0.3$ dex and [Fe/H] of $0.05 - 0.2$ dex. The carbon abundances span from a few hundredths of a dex to -0.14 dex offset for BD+27 2057. Nitrogen abundances are consistent for HIP 71837 and BD+27 2057, although HIP 56194 is offset by ~ 0.14 dex. We find lower O abundances, possibly due to different methodologies used (e.g. the NLTE O triplet compared to the [O I] 6300 Å feature).

Overall, systematic differences are near the 1σ errors of M. Afşar et al. (2012) and likely are due to differences in line selection, line-lists, and model atmospheres. The most discrepant parameter is $\log(g)$, but that varies in the literature for the three standard stars. L. Wang et al. (2011) found a T_{eff} of 4900 K and a $\log(g)$ of 2.78 dex for HIP 56194, a $\log(g)$ of 2.90 dex derived for HIP 71837 (S. Hekker & J. Meléndez 2007) and a $\log(g)$ of 2.43 for BD+27 2057 from APOGEE (H. Jönsson et al. 2020).

The carbon isotope ratios are slightly higher than those found in M. Afşar et al. (2012) for HIP 71837 and HIP 56194, however neither $^{12}\text{C}/^{13}\text{C}$ ratio measurement is more than 2σ different. The likely issue is continuum placement for such weak lines. Importantly, the two stars (HIP 56194 and HIP 71837) with high $^{12}\text{C}/^{13}\text{C}$ ratio measurements are easily distinguished compared to the low $^{12}\text{C}/^{13}\text{C}$ ratio star BD+27 2057.

We selected all RHB/RC and RC stars from M. Afşar et al. (2012) and compared their [C/Fe] and [N/Fe] abundances to our results. The results are shown in Fig. 2. Most of the M. Afşar et al. (2012) RC targets are metal-rich, thin disk stars. We find agreement between those abundance ratios and our young, α -rich thin disk RC stars.

4.2. Comparison to LAMOST Parameters

We compare the results from the BACCHUS pipeline with those from the RC catalog of Y. Huang et al. (2020) in Fig 3. We do not measure the total α -element abundance in our sample and so we compare our [Mg/H] abundance to their $[\alpha/\text{H}]$ measurements as a consistency check on identifying α -enriched stars. Our Fe and Mg abundances are normalized by the E. Magg et al. (2022)

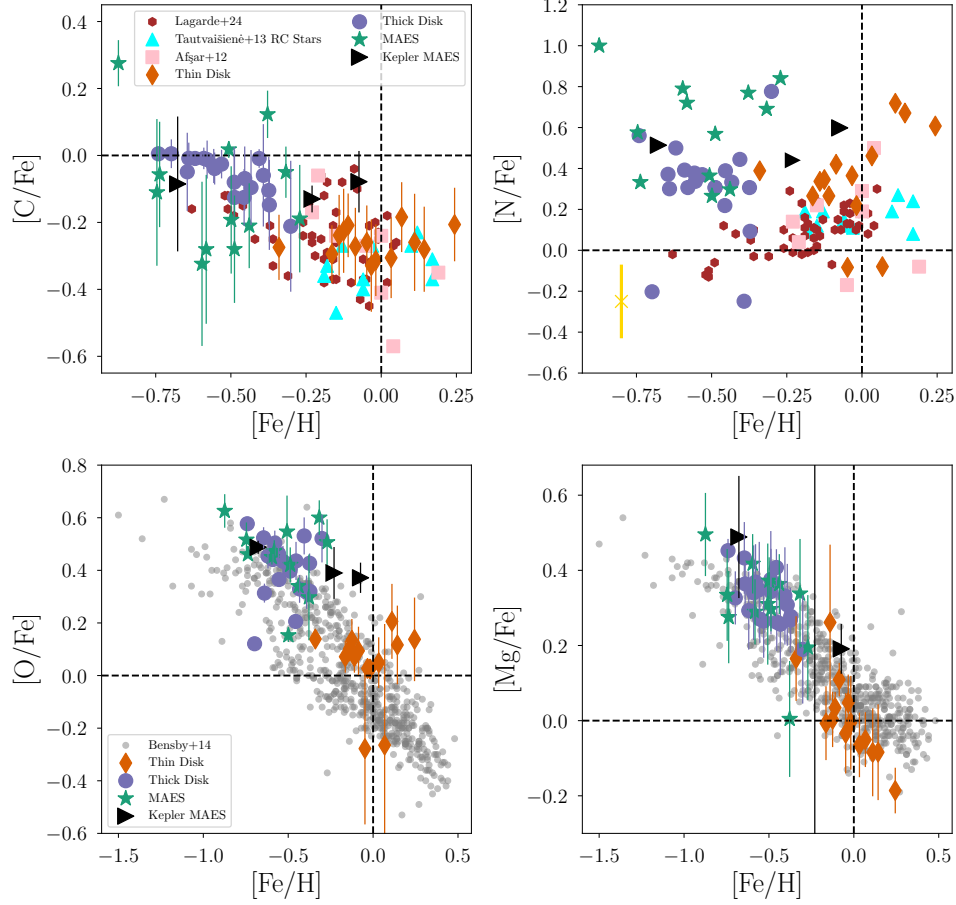


Figure 2. C, N, O, and Mg abundances are plotted for the RC stars in our sample. Representative error bars for $[N/Fe]$ measurements are shown in the gold cross. Most symbols are the same as Fig. 1 with the addition of Kepler MAES targets added as black triangles. The top two panels include $[C/Fe]$ ratios and $[N/Fe]$ ratios of probable RC stars from *M. Afşar et al. (2012)* as pink squares, *N. Lagarde et al. (2024)* as brown hexagons, and *G. Tautvaišienė et al. (2013)* as cyan triangles. The bottom two panels include O and Mg abundances from *T. Bensby et al. (2014)*, represented as gray circles. Red giant abundances are discussed in section 5.4.

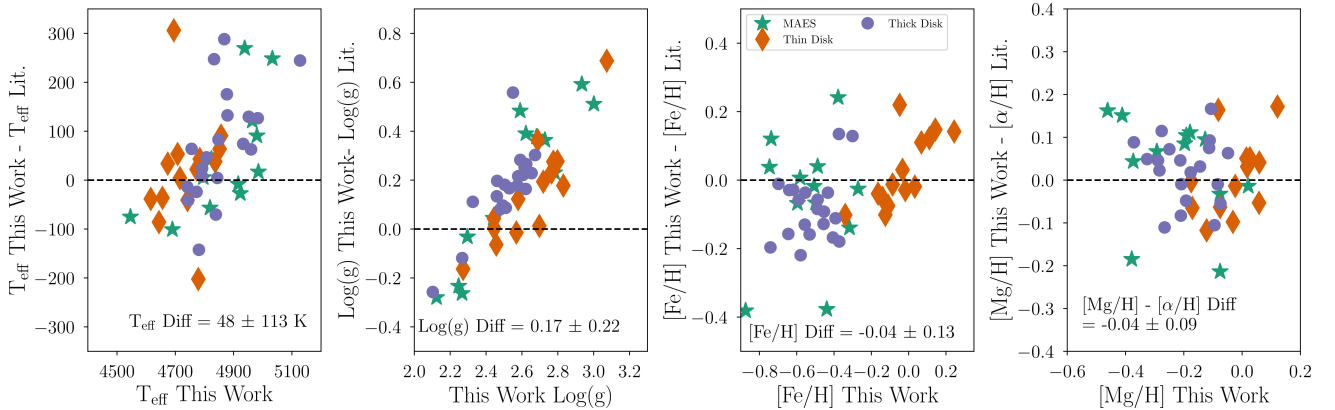


Figure 3. Atmospheric parameter comparison from Table 3 with LAMOST parameters from *Y. Huang et al. (2020)*. The symbols are the same as Fig. 1 and the dashed line represents no difference between the LAMOST value and our measurement.

solar scale and the *Y. Huang et al. (2020)* abundances are not altered.

The average difference and standard deviation were calculated for each star in our sample and listed in Fig.

Table 4. Standard Star Parameters and Abundances

Name	Date Observed	SNR per pixel	T_{eff} (K)	$\log(g)$ (dex)	[Fe/H] (dex)	ξ (kms^{-1})	[C/H]	[N/H]	[O/H]	$^{12}\text{C}/^{13}\text{C}$
From <i>M. Afşar et al. (2012)</i>										
HIP 56194	-	-	4970	2.70	0.15	1.20	-0.33	0.50	0.03	$20 +7/-5$
HIP 71837	-	-	4900	2.60	-0.15	1.10	-0.57	0.29	0.00	15 ± 3
BD+27 2057	-	-	4810	2.25	-0.51	1.25	-0.83	-0.44	-0.16	$5 +2/-1$
This Work										
HIP 56194	2021 Jan 23	108	5000	2.88	-0.03	1.36	-0.34	0.37	-0.01	23 ± 4
HIP 56194	2021 Feb 21	108	5010	2.99	-0.03	1.37	-0.30	0.36	-0.03	28 ± 5
HIP 56194	2022 Mar 13	138	5015	2.98	0.01	1.42	-0.31	0.35	-0.02	25 ± 4
HIP 71837	2021 Feb 22	165	5030	2.73	-0.3	1.65	-0.53	0.29	-0.14	26 ± 4
HIP 71837	2021 Apr 25	152	4929	2.68	-0.27	1.38	-0.56	0.23	-0.08	23 ± 3
HIP 71837	2022 Mar 12	167	4941	2.86	-0.27	1.37	-0.50	0.29	-0.01	23 ± 3
BD+27 2057	2021 Jan 22	153	4873	2.34	-0.56	1.35	-0.69	-0.39	-0.23	5 ± 1

Solar Abundance Scale from *E. Magg et al. (2022)* for our work. We do not re-normalize results reported from *M. Afşar et al. (2012)* since they derived differing solar abundances on a species by species basis using their own solar spectrum.

3. Typical uncertainties for the LAMOST values are 100 K, 0.1 dex, and 0.05 dex for T_{eff} , $\log(g)$, [Fe/H], and $[\alpha/\text{H}]$ (*A. L. Luo et al. 2015; M. S. Xiang et al. 2015, 2017; Y. Huang et al. 2020*). If we assume the total scatter is a combination of uncorrelated BACCHUS and LAMOST catalog errors, then the uncertainties for our sample would be 53 K, 0.2 dex, 0.08 dex, and 0.04 dex for T_{eff} , $\log(g)$, [Fe/H], and [Mg/H].

Only our measured surface gravity is offset relative to the measurements from *Y. Huang et al. (2020)* and has significant uncertainty. Our repeated measurements described in section 4.1 show that internal consistency for $\log(g)$ measurements are on the order of 0.1 - 0.2 dex, consistent with uncertainties estimated from the LAMOST comparisons. Additionally, the LAMOST $\log(g)$ values were derived using asteroseismic training samples which can have systematic differences from spectroscopically derived $\log(g)$ on the order of 0.1 - 0.2 dex depending on spectral type (*M. H. Pinsonneault et al. 2014; M. S. Xiang et al. 2017; N. Lagarde et al. 2024*). Similar changes in systematic offsets that change with $\log(g)$ and T_{eff} have also been observed when comparing LAMOST values to APOGEE abundances (*M. S. Xiang et al. 2017; A. Y. Q. Ho et al. 2017*). Although the $\log(g)$ values are offset, the carbon isotope ratio is minimally sensitive to changes in atmospheric parameters. For example, *N. Lagarde et al. (2024)* finds a change of $\log(g) = 0.22$ dex has an offset of $\Delta ^{12}\text{C}/^{13}\text{C} = \pm 1$ using the CN line, *G. Tautvaišienė et al. (2013)* finds varying the $\log(g)$ by +0.3 dex led to $\Delta ^{12}\text{C}/^{13}\text{C}$ between -2 and 0 using the CN line, and *Z. G. Maas et al. (2019)* found a change of 0.2 dex for $\log(g)$ created an average $\Delta ^{12}\text{C}/^{13}\text{C} = 0.1$ using CO lines. Changes with other atmospheric parameters are also found to offset the carbon isotope ratio by $\Delta ^{12}\text{C}/^{13}\text{C} \sim 1\text{-}2$ (*N. Lagarde et al. 2024*)

4.3. Other Literature Comparisons

We compare our derived Mg and O abundances with literature FGK stars from *T. Bensby et al. (2014)* in Fig. 2. We expect the [O/Fe] and [Mg/Fe] vs. [Fe/H] relationship to match known Milky Way chemical evolution patterns, while C and N may be uniquely affected by evolutionary state for RC stars. The abundances of *T. Bensby et al. (2014)* were placed on the abundance scale *E. Magg et al. (2022)*. We find broad agreement between our abundance ratios and those of *T. Bensby et al. (2014)*, further demonstrating the reliability of our abundance measurement methodology.

Lastly, we compared our C and N abundances to red clump stars from *M. Afşar et al. (2012); N. Lagarde et al. (2024)* in Fig. 2. Our carbon abundances are similar to the literature abundances for both stellar populations. For N, our abundances are $\sim 0.1\text{-}0.3$ dex higher for both stellar populations, with the most metal-poor *N. Lagarde et al. (2024)* stars are the most offset from our results. The abundances may differ due to different abundance analysis methodologies. For example, we fit all CN lines simultaneously and used the oxygen triplet to determine O abundances. *N. Lagarde et al. (2024)* used the [O I] 6300.31 Å when available (and used Mg as a proxy for O when the [O I] feature was telluric contaminated) and fit seven strong CN features individually.

4.4. Final Uncertainties

Final abundances and reported uncertainties in table 5 were derived from the mean abundance and standard deviation on abundances from the set of lines available for each element. Two exceptions are the nitrogen uncertainty and the $^{12}\text{C}/^{13}\text{C}$ ratio uncertainty. The nitrogen abundance was fit from multiple lines simulta-

neously and carbon isotope ratio uncertainty is derived from repeated measurements.

We expect the SNR-statistical uncertainty to be the most significant source of uncertainty due to the weak ^{13}C line strengths. The carbon isotope ratio uncertainties were derived from a Monte Carlo simulation to best characterize the errors fitting the one absorption line, 2500 mock observations were generated for each star by treating each point in the observed spectrum as a Gaussian, with a mean value of the observed normalized flux and the standard deviation set by the signal-to-noise ratio of the data. The data was fit using the same χ^2 minimization technique and the 16% and 84 % values were adopted as the 1σ uncertainties reported in Table 5.

5. DISCUSSION

5.1. Star Kinematics and Li Abundance Estimates

We calculate stellar population membership probabilities using UVW velocities since previous studies have used full 6-d phase space motion to distinguish between thin and thick disk stars. Kinematics can provide additional verification on population for our age-[α /Fe] classification system, although chemical abundance may provide a cleaner sample selection than kinematics (V. Silva Aguirre et al. 2018). Other studies find MAE stars generally have similar UVW velocities as thick disk stars (W. X. Sun et al. 2020; M. Zhang et al. 2021) and our calculations can help distinguish between formation mechanism and provide evidence of potential sample contamination.

We determined the probabilities using the same methodology as Z. G. Maas et al. (2022). To summarize, we used kinematic information from Gaia Collaboration et al. (2023) with zero-point corrections applied to the parallax values using the calculation from L. Lindgren et al. (2021). UVW velocities and errors were calculated using `pyia` (A. Price-Whelan 2018), coordinate transformations were done with `Astropy` (Astropy Collaboration et al. 2013), and population probabilities from I. Ramírez et al. (2013). Our final UVW velocities are listed in Table 5.

We find that the thin disk and thick disk memberships based on chemistry and age in Fig. 1 are broadly consistent with population assignment based on kinematics. All of our thin disk stars have kinematic probabilities consistent with the chemistry/age selection. For thick disk stars, 10 stars have 50% or higher thick disk membership probability, five stars have a 90% or larger thin disk membership probability, and one thick disk star has a 61% probability of being a halo star.

We also estimated the lithium abundances using the feature at 6707 Å to aid in constraining formation mechanisms of the MAE stars. For example, high Li abundances may be a signal of mergers between red giants and white dwarfs, especially when combined with $^{12}\text{C}/^{13}\text{C}$ ratio measurements (X. Zhang et al. 2020; S. Maben et al. 2023). We used `TSFitPy` to estimate the LTE abundance for each star to determine if any star may be potentially Li-rich, with a threshold of $A(\text{Li}) > 1.5$ dex (e.g. C. Aguilera-Gómez et al. 2023). We found no enhanced Li abundance for any of our MAE stars and only one thin disk star met the criteria and with an estimated $A(\text{Li}) = 1.82$ dex (DR3 4009353280781776384).

5.2. Carbon Isotope Ratios for Red Clump Stars

The $^{12}\text{C}/^{13}\text{C}$ as a function of [Fe/H] and mass are plotted in Fig. 4 for the thin disk, thick disk, and MAE star samples studied in this work. We increased the comparison size by adding literature abundance measurements from M. Afşar et al. (2012); C. Aguilera-Gómez et al. (2023); N. Lagarde et al. (2024). In all samples we chose only HB or RC stars, and stars with probabilities greater than 95% of being in the RC from C. Aguilera-Gómez et al. (2023).

We find that our thin disk stars are generally consistent with other red clump stars near solar metallicities. The only thin disk star with a $^{12}\text{C}/^{13}\text{C}$ ratio above 20 is a mildly Li rich star with $A(\text{Li}) \sim 1.8$ dex, as discussed in subsection 5.1. C. Aguilera-Gómez et al. (2023) found RC stars with Li near ~ 1.5 that also had high $^{12}\text{C}/^{13}\text{C} > 20$, in addition to RC stars with $A(\text{Li}) < 1$ and low Li. Our thick disk sample also appears have decreasing $^{12}\text{C}/^{13}\text{C}$ ratios with decreasing metallicity, although there is significant scatter in the abundances. Overall, the average thin disk isotopic ratio is $\langle ^{12}\text{C}/^{13}\text{C} \rangle = 14.8 \pm 5.2$ and $\langle ^{12}\text{C}/^{13}\text{C} \rangle = 8.2 \pm 3.4$ for thick disk stars. Removing the one Li rich star, with a high carbon isotope ratio leads to an average of $\langle ^{12}\text{C}/^{13}\text{C} \rangle = 13.9 \pm 4.2$ for the thin disk.

While the relationship between $^{12}\text{C}/^{13}\text{C}$ and mass has significant scatter, as shown in Fig. 4, the average difference between thin disk and thick disk stars is similar to the models of N. Lagarde et al. (2012) that include thermohaline mixing. For $Z = 0.014$ (approximately solar metallicity), the 1 solar mass RC model has a $^{12}\text{C}/^{13}\text{C} = 6.6$ and the model with a mass of 1.5 has a $^{12}\text{C}/^{13}\text{C} = 11.8$. Our abundances that sample to lower metallicity evolved stars may help aid in constraining future models of extra-mixing for stars between 0.8 - 2 solar masses.

The statistical methods used to measure star masses may introduce random uncertainties or systematic biases. Underestimated mass uncertainties may result in

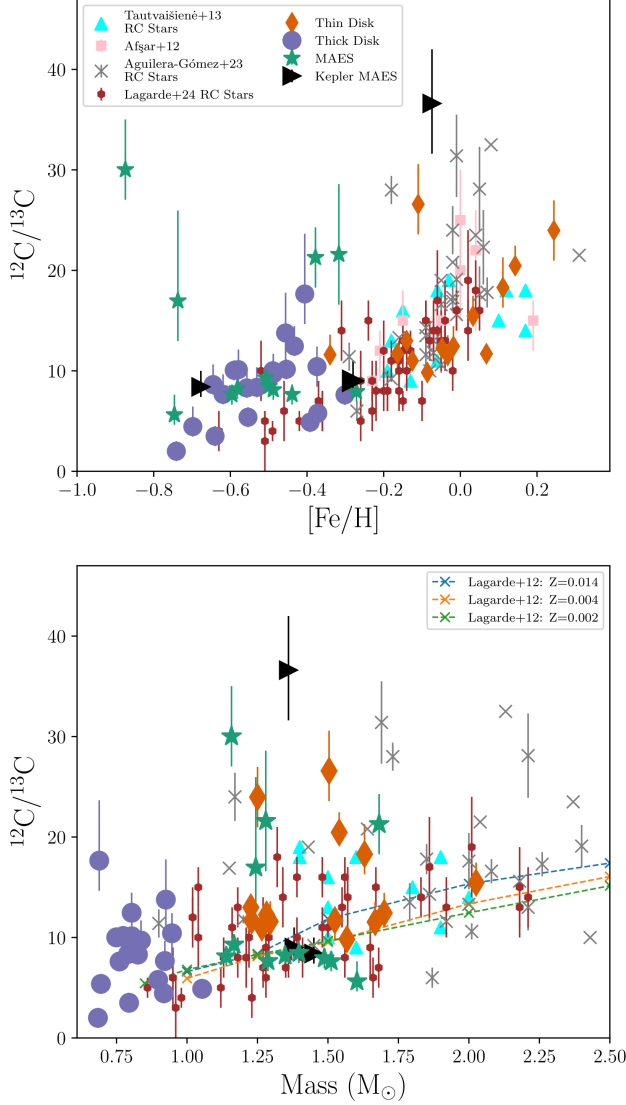


Figure 4. The carbon isotope ratios from our sample stars are plotted with reference to metallicity (left) and the stellar mass (right panel). Masses were adopted from W. X. Sun et al. (2020). The symbols are the same as Fig. 2.

misclassified MAE stars that are likely low-mass thick disk stars. Potential stellar population contamination makes drawing conclusions on typical $^{12}\text{C}/^{13}\text{C}$ ratios for MAE stars potentially challenging. For systematic errors, a correlation with mass derived from KPCA analysis and $[\text{C}/\text{N}]$ would bias our sample against finding stars from the multiple different pathways MAE stars might form. However, We do find that our MAE stars span a range of $[\text{C}/\text{N}]$, similar to previous studies of MAE stars (S. Hekker & J. A. Johnson 2019).

5.3. MAES RC Stars with Anomalous $^{12}\text{C}/^{13}\text{C}$ Ratios: Possible Formation Pathways

10 out of our 15 red clump MAE stars have carbon isotope ratios consistent with thick disk stars at similar metallicities. Our results are in-line with other studies of thick disk stars that find carbon abundances, kinematics, and α -enrichment for MAE stars are similar to thick disk members (W. X. Sun et al. 2020; M. Zhang et al. 2021; V. Cerqui et al. 2023). However, a small number of our MAE stars have $^{12}\text{C}/^{13}\text{C}$ ratios significantly higher than other red clump stars at similar metallicities. Five stars in total have $^{12}\text{C}/^{13}\text{C} > 15$ and as seen in Fig. 4; four RC stars selected from W. X. Sun et al. (2020); Y. Huang et al. (2020) and one star with a mass identified from asteroseismology. While these stars have different metallicities, none have enhanced Li ratios making some merger scenarios, such as a merger with a white dwarf, unlikely (X. Zhang et al. 2020). The properties of the outlier stars are described below.

KIC 3833399: KIC 3833399 is the high metallicity, carbon isotope ratio outlier, with a mass of $1.48 M_\odot$ (P. Jofré et al. 2023). The carbon isotope ratio is approximately 4σ away from our average carbon isotope ratio of 14.8 for thin disk stars although this star has a 78% chance of belonging to the thin disk population based on kinematics. Additionally, long-term radial velocity monitoring from P. Jofré et al. (2023) found no evidence that KIC 3833399 had a binary companion. A stellar merger scenario must have increased the total mass and increased the surface $^{12}\text{C}/^{13}\text{C}$ ratio while not enhancing the total $[\text{C}/\text{Fe}]$ abundance which may be expected from mass-transfer with an AGB companion. Another possibility is that this massive star is genuinely young as evidenced from the high $^{12}\text{C}/^{13}\text{C}$ and kinematic classification; a scenario suggested for other MAE stars (Y. Lu et al. 2024).

Gaia DR3 672933143771515392: Gaia DR3 672933143771515392 is the most metal poor star in the sample with an $[\text{Fe}/\text{H}] = -0.87$, a $^{12}\text{C}/^{13}\text{C}$ ratio of 30 ± 5 , and a 89% probability of being a thick disk member. The star also has high carbon and nitrogen abundances with $[\text{C}/\text{Fe}] = 0.28$ dex and $[\text{N}/\text{Fe}] = 1.00$ compared to other MAE stars. This star was also identified as a CH star from LAMOST spectra with enhanced CH lines in the G band, CN at 4215 Å, and Ba II features (W. Ji et al. 2016). Mass-transfer with an AGB star companion may explain these abundance patterns since AGB stars have enhanced ^{12}C and N abundances (V. V. Smith & D. L. Lambert 1990). Gaia DR3 672933143771515392 appears to be an RC star that previously had an AGB star companion and additional s-process element abun-

dance ratios may further constrain the mass of the potential companion.

Gaia DR3 638939267896892800: Gaia DR3 638939267896892800 is both kinematically similar to thin disk stars and has a $^{12}\text{C}/^{13}\text{C} = 21 \pm 3$ which is $\sim 2\sigma$ away from the average thin disk carbon isotope ratio. LAMOST spectra also identified this star as a CH star (W. Ji et al. 2016). J. Shejeelammal et al. (2021) finds a lower metallicity $[\text{Fe}/\text{H}] = -0.53$ and a higher carbon abundance of $[\text{C}/\text{Fe}] = 0.23$ (after adjusting the solar normalization to match our value of $A(\text{C})|_{\odot} = 8.56$). Our carbon abundance of $[\text{C}/\text{Fe}] = 0.12$ is enhanced relative to other RC stars and consistent within the uncertainties with J. Shejeelammal et al. (2021). Overall, this star has CNO abundances consistent with mass transfer with an AGB companion.

Gaia DR3 3671355056986858880: Gaia DR3 3671355056986858880 was measured to have an $[\text{Fe}/\text{H}] = -0.32$ and a $^{12}\text{C}/^{13}\text{C} = 22^{+7}_{-5}$. The $^{12}\text{C}/^{13}\text{C}$ ratio is 2.75σ higher than the average thick disk carbon isotope ratio. Unlike the previous anomalous stars, this object is not well-studied in the literature. We do not find an increased carbon abundance ($[\text{C}/\text{Fe}] = -0.05$) suggesting mass-transfer with an AGB companion is not as likely as other stars with high $^{12}\text{C}/^{13}\text{C}$ ratios in our sample. Data from Gaia DR3 finds no obvious sign of binarity; the star has a RUWE of 1.05 and a Gaia DR3 radial velocity error of 0.26 km s^{-1} (Gaia Collaboration et al. 2023). The kinematic analysis suggests that this star is a likely thick disk member and the binary interaction that created the mass enhancement must have happened in a manner that allowed the carbon isotope ratio to be consistent with a higher mass star.

The abundances are also consistent with a sub-giant star that is undergoing the first dredge-up. The potential the star is misclassified is unlikely since both the atmospheric parameters and photometry in Fig. 1 show that Gaia DR3 3671355056986858880 are consistent with an RC star. Alternatively, the star may be heated by other temporary properties that would make a sub-giant star bluer and more luminous. Temporary tidal heating may affect stars in open cluster (S. J. Arthur et al. 2024) can cause a similar effect. However, tidal heating would move energy from the orbit and cause stellar mergers. The high kinematic probability of being a thick disk star would suggest that we are not catching the star in a rare instance of tidal heating and longer-term radial velocity monitoring and s-process abundance measurements would shed light on the origins of this star. Large changes to the inner structure happen when two stars merge. For example, a star created through a stellar merger is expected to have over-

massive envelopes relative to their core masses compared to similar mass single stars (N. Z. Rui & J. Fuller 2021). The high $^{12}\text{C}/^{13}\text{C}$ ratio may aid in constraining models of stars created through full merger scenarios.

Gaia DR3 971925848973504512: Gaia DR3 971925848973504512 has a $^{12}\text{C}/^{13}\text{C} = 17^{+9}_{-4}$ which is approximately 2σ higher than other stars at similar metallicities near $[\text{Fe}/\text{H}] = -0.74$. However, the star is otherwise similar to low-mass thick disk stars chemically and kinematically. This star has no large enhancement of carbon or nitrogen and has a 93% probability of being a thick disk star. The star has a RUWE of 0.96 and no large RV uncertainties from Gaia DR3 (Gaia Collaboration et al. 2023) suggesting the object is not in a binary system. The isotope ratio seems consistent for a single-star evolution of a $1.5 M_{\odot}$. This star may have undergone a stellar merger before either object evolved off the main sequence. Additionally, the measurement is only 2σ from similar thick disk stars and may be explained by statistical uncertainties within the carbon isotope ratio measurement.

5.4. Carbon Isotope Ratios for Red Giant Stars

We also observed a small sample of stars identified as MAES stars on the RG branch. Since the $^{12}\text{C}/^{13}\text{C}$ ratio changes as a red giant evolves, we cannot directly compare the surface composition of these objects to our RC sample. Specifically, the carbon isotope ratio depends strongly on position on the red giant branch and on initial metallicity. The first dredge up initially lowers the $^{12}\text{C}/^{13}\text{C}$ to values near 30-40 and additional mixing occurs after the LF bump, decreases the value further. We therefore compare our results to literature sources of open clusters (C. McCormick et al. 2023), globular clusters (G. H. Smith et al. 2007), and disk stars (L. D. Keller et al. 2001; G. Tautvaišienė et al. 2013; C. Aguilera-Gómez et al. 2023) in Fig. 5.

We find that three of our Kepler MAE stars have carbon isotope ratios similar to stars at similar metallicities and evolutionary states. However, the star KIC5966873 has a high $^{12}\text{C}/^{13}\text{C}$, that is comparable to high-metallicity open cluster members of G. Tautvaišienė et al. (2013). The high carbon isotopic ratio suggests that extra-mixing has not yet begun in KIC 5966873 or that there has been mass-transfer of ^{12}C -rich material. This star does not have an unusual CNO abundances relative to the other Kepler red giant stars, suggesting that the source of the mass-transfer from a carbon rich object is unlikely. Our limited sample inhibits definitive descriptions on the formation pathway of this object but additional carbon isotope ratio mea-

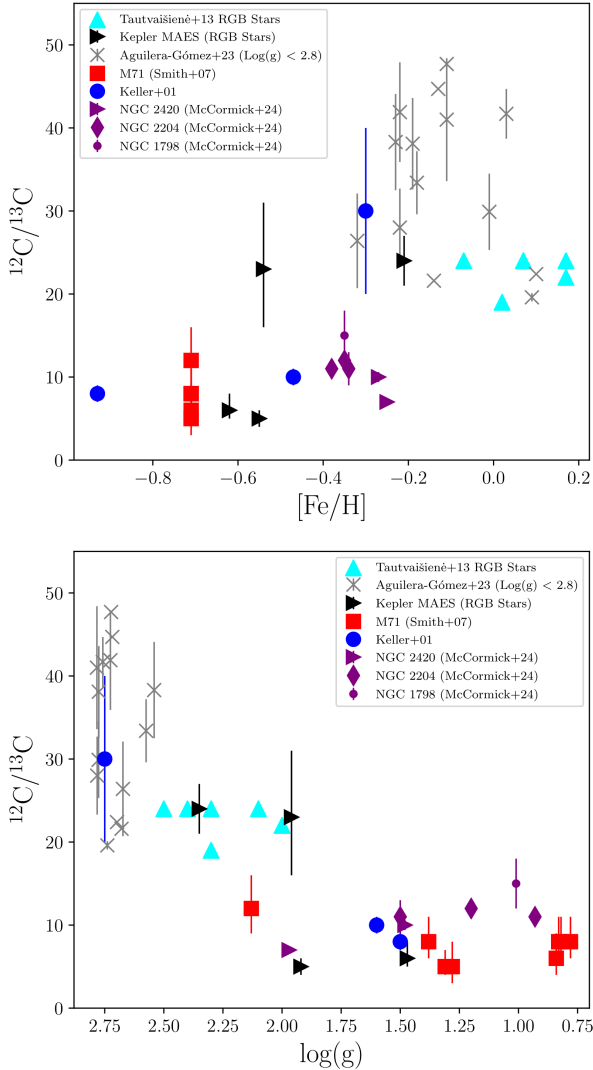


Figure 5. The carbon isotope ratios from our sample stars are plotted with reference to metallicity (left) and the surface gravity (right panel). The symbols are the same as Fig. 2. The solid points are stars within the RC photometric sample (shown in Fig. 1).

measurements of red giant stars will shed light on if this star is truly an outlier.

6. CONCLUSIONS

We explored the origins of MAE stars by measuring the carbon isotope ratios for red clump stars identified from LAMOST data (Y. Huang et al. 2020; W. X. Sun et al. 2020) and in stars with asteroseismic masses determined from Kepler observations. Abundance analysis was conducted with Turbospectrum using both the TSFitpy and BACCHUS codes. Overall, we measured metallicities, CNO abundances, and carbon isotope ratios in 19 MAE stars (15 red clump stars and four red giant stars), 14 thin disk stars, and 20 thick disk stars.

10 of the red clump MAE stars had similar carbon isotope ratios, between $6 < ^{12}\text{C}/^{13}\text{C} < 8$, to thick disk stars at similar metallicities. Carbon isotope ratios were not found near the CNO burning equilibrium of 3.5 that is observed when significant amount of material is dredged up for metal-poor red giants beyond the luminosity function bump. Additionally, some of the MAE stars have similar isotope ratios seen in single low mass stars and five of the red clump MAE stars have high $^{12}\text{C}/^{13}\text{C}$ ratios between 17 - 37. These stars span a metallicity range of $-0.87 < [\text{Fe}/\text{H}] < -0.07$. Two of the anomalous stars appear have $[\text{C}/\text{Fe}]$ and $[\text{N}/\text{Fe}]$ abundance ratios consistent with mass-transfer from an AGB star companion. The other three stars have no signatures of binarity and the carbon isotope ratio may constraints on potential merger scenarios.

We find three MAE red giant stars have carbon isotope ratios consistent with other giants studied in the literature at similar metallicities and surface gravities. However, one red giant, KIC 5966873, has a $^{12}\text{C}/^{13}\text{C}$ ratio of 23^{+8}_{-7} , around $\sim 2\sigma$ larger than similar red giants. The carbon isotope ratio better resembles high metallicity red giant stars and the $^{12}\text{C}/^{13}\text{C}$ ratio may constrain the formation mechanism of this MAE star. Overall, the carbon isotope ratio may provide a unique constraint on the evolutionary history of MAE stars and distinguish between different formation pathways.

ACKNOWLEDGMENTS

We thank the referee for their thoughtful feedback and suggestions that improved this manuscript. This work has made use of data from the European Space Agency (ESA) mission *Gaia* (<https://www.cosmos.esa.int/gaia>), processed by the *Gaia* Data Processing and Analysis Consortium (DPAC, <https://www.cosmos.esa.int/web/gaia/dpac/consortium>). Funding for the DPAC has been provided by national institutions, in particular the institutions participating in the *Gaia* Multilateral Agreement. This paper includes data taken at The McDonald Observatory of The University of Texas at Austin. This research has made use of the SIMBAD database, operated at CDS, Strasbourg, France. This research has made use of the VizieR catalogue access tool, CDS, Strasbourg Astronomical Observatory, France (DOI : 10.26093/cds/vizier). We thank Gloria Koenigsberger for excellent discussions on this research that improved the manuscript. ZGM is partially supported by a NASA ROSES-2020 Exoplanet Research Program Grant (20-XRP20 2-0125). CM is supported by the NSF Astronomy and Astrophysics Fellowship award number AST-2401638. KH is partially supported

through the NSF Astronomy and Astrophysics Grants AST-2407975 and AST-2108736 along with the Wootton Center for Astrophysical Plasma Properties funded under the United States Department of Energy collaborative agreement DE-NA0003843.

Facilities: McDonald Observatory: 2.7 m Harlan J. Smith Telescope (Tull Coudé)

Software: `scipy` (P. Virtanen et al. 2020), `numpy` (C. R. Harris et al. 2020), `matplotlib` (J. D. Hunter

2007), `astropy` (Astropy Collaboration et al. 2013, 2018, 2022), `pyia` (A. Price-Whelan 2018), `dustmaps` (G. M. Green et al. 2019), `iSpec` (S. Blanco-Cuaresma et al. 2014; S. Blanco-Cuaresma 2019), `Turbospectrum` (B. Plez 2012), and `TSFitPy` (J. M. Gerber et al. 2023; N. Storm & M. Bergemann 2023)

APPENDIX

A. APPENDIX 1: STAR INFORMATION

The full abundance information for our sample is listed in Table 5 in this appendix.

Table 5. Abundances and Kinematics for Sample Stars

Gaia DR3 ID	[Fe/H]	[C/Fe]	σ [C/Fe]	[N/Fe]	[O/Fe]	σ [O/Fe]	[Mg/Fe]	σ [Mg/Fe]	$\frac{12\text{C}}{13\text{C}}$	σ $\frac{12\text{C}}{13\text{C}}$	U	V	W	σ U	σ V	σ W	P(Thin)	P(Thick)	P(Halo)	
	(dex)	(dex)	(dex)	(dex)	(dex)	(dex)	(dex)	(dex)	$\frac{12\text{C}}{13\text{C}}$	σ $\frac{12\text{C}}{13\text{C}}$	(kms^{-1})	(kms^{-1})	(kms^{-1})	(kms^{-1})	(kms^{-1})	(kms^{-1})				
Thin Disk																				
866507457241940480	-0.02	-0.31	0.11	0.22	0.02	0.01	-0.01	0.12	12	2	1	-29.35	-22.75	14.28	0.14	0.18	0.11	0.98	0.02	0.00
688166190179213184	0.11	-0.26	0.15	0.72	0.21	0.14	-0.08	0.12	18	3	2	12.96	8.42	0.12	0.13	0.06	0.12	0.99	0.01	0.00
3138549726673657600	0.03	-0.31	0.12	0.46	0.05	0.10	-0.06	0.09	15	2	1	-12.42	31.03	9.71	0.25	0.33	0.06	0.98	0.02	0.00
4009353280781776384	-0.11	-0.21	0.10	0.27	0.07	0.06	0.03	0.04	27	4	3	22.25	-16.45	-11.52	0.11	0.33	0.16	0.99	0.01	0.00
1312079562236150656	-0.03	-0.33	0.14	0.36	0.03	0.01	0.05	0.07	12	2	1	28.19	12.23	-24.08	0.16	0.12	0.21	0.98	0.02	0.00
1388620891675799168	-0.16	-0.29	0.09	0.27	0.07	0.06	-0.01	0.10	12	1	2	-20.95	-18.75	-14.85	0.12	0.07	0.11	0.99	0.01	0.00
3833688568619253120	0.14	-0.28	0.13	0.67	0.12	0.15	-0.08	0.13	20	2	1	-5.80	-19.31	3.67	0.12	0.14	0.18	0.99	0.01	0.00
842398878096774784	-0.05	-0.26	0.11	-0.08	-0.28	0.29	-0.03	0.11	12	1	1	22.34	-32.75	-22.11	0.11	0.28	0.12	0.96	0.04	0.00
1330490025449104640	-0.12	-0.23	0.13	0.35	0.13	0.08	0.00	0.07	11	1	1	-46.64	35.82	-0.81	0.31	0.21	0.10	0.97	0.03	0.00
3326023296796724096	0.24	-0.21	0.11	0.61	0.14	0.16	-0.19	0.06	24	3	3	-1.69	-31.29	-0.61	0.18	0.28	0.10	0.98	0.02	0.00
3976449776845278592	-0.09	-0.27	0.12	0.42	0.09	0.09	0.11	0.04	10	1	1	-21.77	-53.62	-1.22	1.14	1.84	1.00	0.88	0.12	0.00
3976085529258764800	0.07	-0.18	0.10	-0.08	-0.26	0.46	-0.05	0.07	12	1	1	-24.36	-10.48	-9.29	0.36	0.18	0.18	0.99	0.01	0.00
1486503509885506944	-0.34	-0.27	0.10	0.39	0.14	0.04	0.17	0.11	12	2	1	70.26	-4.29	29.09	0.49	0.22	0.25	0.96	0.04	0.00
1447162502806921472	-0.14	-0.24	0.12	0.34	0.10	0.05	0.26	0.21	13	1	1	13.08	11.73	-20.89	0.08	0.07	0.12	0.99	0.01	0.00
Thick Disk																				
3130104824535988096	-0.49	-0.13	0.14	0.31	0.41	0.02	0.34	0.11	10	2	1	2	-57.34	-46.81	0.48	0.62	0.69	0.41	0.58	0.01
3222153253655970176	-0.55	-0.04	0.05	0.34	0.37	0.00	0.27	0.06	5.00	1	1	54.03	-31.23	10.05	0.29	0.58	0.10	0.96	0.04	0.00
1544130323049089536	-0.39	-0.06	0.15	-0.25	0.32	0.06	0.31	0.11	5	1	1	23.68	-70.85	25.62	0.13	1.00	0.40	0.33	0.66	0.01
723448831119162752	-0.59	-0.01	0.03	0.39	0.44	0.02	0.34	0.13	10	1	1	1.19	-52.37	-35.37	3.02	2.91	6.61	0.74	0.26	0.00
309660828405802240	-0.41	-0.01	0.03	0.44	0.53	0.07	0.33	0.13	18	6	3	21.25	12.23	-29.09	0.18	0.13	0.45	0.98	0.02	0.00
3811610203335180416	-0.64	-0.01	0.05	0.30	0.31	0.04	0.36	0.06	4	1	1	64.44	-75.80	21.05	0.78	0.78	0.39	0.13	0.86	0.02
1295525109008882816	-0.37	-0.15	0.13	0.09	0.32	0.03	0.28	0.07	6	1	1	-47.18	0.71	-31.13	0.68	0.27	0.21	0.97	0.03	0.00
3941980190394162560	-0.45	-0.07	0.10	0.39	0.44	0.07	0.26	0.08	10	1	1	201.57	-68.33	-62.93	4.26	1.79	0.59	0.00	0.39	0.61
3869545635666293504	-0.43	-0.10	0.11	0.33	0.33	0.05	0.26	0.14	12	2	1	-7.55	-101.29	-30.84	0.25	1.63	1.06	0.00	0.96	0.03
3283445774160853632	-0.74	0.01	0.02	0.56	0.58	0.02	0.45	0.03	2	1	1	-63.73	-83.45	7.21	0.21	0.96	0.48	0.06	0.92	0.02
1244397371640334080	-0.53	-0.03	0.04	0.37	0.43	0.06	0.26	0.10	8	2	1	-23.07	-36.04	7.91	0.48	0.64	0.24	0.97	0.03	0.00
640282939825239936	-0.56	-0.03	0.05	0.38	0.46	0.03	0.35	0.13	8	2	1	13.44	-70.03	-10.41	0.12	0.81	0.34	0.50	0.50	0.00
400886727292925824	-0.62	-0.01	0.02	0.50	0.45	0.05	0.29	0.10	8	2	1	-6.99	-75.77	27.94	0.18	0.82	0.18	0.20	0.79	0.01
3882249324293741440	-0.58	-0.01	0.06	0.31	0.50	0.05	0.37	0.10	10	2	2	59.35	-34.19	37.38	1.07	0.54	0.23	0.85	0.15	0.00
3723876425343292032	-0.70	0.01	0.04	-0.20	0.12	0.01	0.33	0.07	4	2	1	-107.23	-71.60	48.92	1.99	1.34	0.72	0.01	0.94	0.05
3973325544619220224	-0.65	-0.05	0.12	0.37	0.52	0.04	0.43	0.10	9	2	1	49.83	-153.31	-5.69	0.71	2.43	0.74	0.00	0.61	0.39
3896192196887050368	-0.30	-0.21	0.20	0.78	0.52	0.09	0.19	0.14	8	1	1	-28.18	-45.50	-31.99	0.84	1.14	0.61	0.85	0.15	0.00
3163974593033517824	-0.46	-0.13	0.08	0.22	0.21	0.02	0.41	0.05	14	4	3	-70.37	-37.08	-75.67	0.48	0.25	1.38	0.06	0.90	0.04
3813076676968705408	-0.49	-0.08	0.10	0.31	0.40	0.03	0.38	0.13	10	1	1	-82.83	-37.09	45.77	1.22	0.28	0.43	0.54	0.45	0.01
1275573508452428288	-0.37	-0.10	0.10	0.31	0.43	0.04	0.27	0.09	10	2	2	62.26	6.23	8.16	0.59	0.13	0.24	0.98	0.02	0.00
MAES																				
672933143771515392	-0.87	0.28	0.07	1.00	0.63	0.06	0.50	0.11	30	5	3	-29.14	-61.32	-60.73	0.35	1.01	1.40	0.09	0.89	0.02
638939267896892800	-0.38	0.12	0.07	0.77	0.30	0.16	0.00	0.15	21	3	3	-10.46	-2.62	6.61	0.35	0.13	0.38	0.99	0.01	0.00
607150428232731008	-0.51	0.02	0.03	0.36	0.55	0.14	0.31	0.16	9	1	1	-51.78	-80.73	8.54	0.13	0.40	0.40	0.12	0.87	0.01
579491624824868608	-0.27	-0.19	0.16	0.84	0.51	0.09	0.19	0.14	8	1	1	-0.26	-20.40	-3.51	0.72	1.13	1.45	0.99	0.01	0.00

Table 5 continued

Table 5 (*continued*)

Gaia DR3 ID	[Fe/H]	[C/Fe]	σ	[C/Fe]	[N/Fe]	[O/Fe]	[Mg/Fe]	σ	$\frac{12\text{C}}{13\text{C}}$	σ	$\frac{12\text{C}}{13\text{C}}$	U	V	W	σ U	σ V	σ W	P(Thin)	P(Thick)	P(Halo)
	(dex)	(dex)	(dex)	(dex)	(dex)	(dex)	(dex)	(dex)	High	Low	σ	(km s^{-1})	(km s^{-1})	(km s^{-1})	(km s^{-1})	(km s^{-1})	(km s^{-1})			
1235499505072865792	-0.44	-0.21	0.13	0.30	0.34	0.02	0.36	0.08	8	1	1	34.81	-55.49	-15.08	0.27	0.53	0.18	0.80	0.19	0.00
971925848975504512	-0.74	-0.06	0.16	0.33	0.46	0.01	0.28	0.12	17	9	4	0.61	-89.50	11.90	0.34	0.97	0.09	0.05	0.93	0.02
3872367429179326592	-0.58	-0.28	0.22	0.72	0.47	0.04	0.29	0.09	8	1	1	4.03	-114.72	-83.23	0.39	2.96	1.72	0.00	0.76	0.24
636614659798851712	-0.60	-0.32	0.25	0.79	0.45	0.03	0.42	0.08	8	1	1	-122.42	-54.48	-91.04	1.61	0.68	2.20	0.00	0.77	0.23
685849244302001408	-0.49	-0.28	0.16	0.57	0.42	0.07	0.30	0.06	8	1	1	118.26	-47.90	-11.66	0.82	1.16	0.34	0.41	0.57	0.02
387628079296214272	-0.50	-0.19	0.16	0.27	0.15	0.03	0.37	0.06	8	2	1	42.27	-46.60	-38.88	0.35	1.00	0.53	0.73	0.27	0.00
3878388801529524480	-0.75	-0.11	0.22	0.58	0.52	0.07	0.33	0.12	6	2	1	15.86	-29.34	70.66	0.86	0.18	0.48	0.34	0.64	0.01
3671355056986858880	-0.32	-0.05	0.08	0.69	0.60	0.07	0.34	0.15	22	7	5	-76.01	-84.87	62.72	1.74	1.61	0.70	0.00	0.93	0.07
Kepler Red Clump MAES																				
2100234510918046592	-0.07	-0.08	0.09	0.60	0.37	0.06	0.19	0.07	37	6	5	-8.24	-56.70	21.89	0.05	0.13	0.19	0.78	0.21	0.00
2117411734401094528	-0.68	-0.09	0.20	0.51	0.49	0.02	0.49	0.16	8	2	1	102.90	-19.10	0.19	0.71	0.26	0.09	0.91	0.09	0.00
2130894220860474752	-0.23	-0.13	0.04	0.44	0.39	0.10	9	2	1	70.70	-37.82	-34.81	0.79	0.42	0.37	0.79	0.21	0.00
Kepler Red Giant MAES																				
2077396108227657344	-0.16	-0.08	0.08	0.36	0.27	0.05	0.01	0.04	24	3	3	3.53	-37.11	-3.15	0.13	0.29	0.10	0.97	0.03	0.00
2100961185027552384	-0.50	-0.37	0.12	0.60	0.41	0.20	0.15	0.05	5	1	1	24.52	-0.43	54.76	0.20	0.29	0.82	0.88	0.12	0.00
2103822354798961280	-0.57	-0.12	0.14	0.50	0.73	0.25	0.15	0.10	6	2	1	22.65	9.50	-43.56	0.25	0.24	0.86	0.95	0.05	0.00
2077396108227657344	-0.49	-0.19	0.13	0.56	0.53	0.22	0.12	0.06	23	8	7	-20.98	-64.83	8.79	0.15	0.19	0.15	0.65	0.34	0.00

NOTE—Note: Solar Abundance Scale from E. Magg et al. (2022)

REFERENCES

- Afşar, M., Sneden, C., & For, B. Q. 2012, *AJ*, 144, 20, doi: [10.1088/0004-6256/144/1/20](https://doi.org/10.1088/0004-6256/144/1/20)
- Aguilera-Gómez, C., Jones, M. I., & Chanamé, J. 2023, *A&A*, 670, A73, doi: [10.1051/0004-6361/202244518](https://doi.org/10.1051/0004-6361/202244518)
- Arthur, S. J., Koenigsberger, G., Brady, K., Estrella-Trujillo, D., & Pilachowski, C. 2024, *ApJ*, 967, 69, doi: [10.3847/1538-4357/ad3cd4](https://doi.org/10.3847/1538-4357/ad3cd4)
- Astropy Collaboration, Robitaille, T. P., Tollerud, E. J., et al. 2013, *A&A*, 558, A33, doi: [10.1051/0004-6361/201322068](https://doi.org/10.1051/0004-6361/201322068)
- Astropy Collaboration, Price-Whelan, A. M., Sipőcz, B. M., et al. 2018, *AJ*, 156, 123, doi: [10.3847/1538-3881/aabc4f](https://doi.org/10.3847/1538-3881/aabc4f)
- Astropy Collaboration, Price-Whelan, A. M., Lim, P. L., et al. 2022, *ApJ*, 935, 167, doi: [10.3847/1538-4357/ac7c74](https://doi.org/10.3847/1538-4357/ac7c74)
- Bailer-Jones, C. A. L., Rybizki, J., Fouesneau, M., Demleitner, M., & Andrae, R. 2021, *AJ*, 161, 147, doi: [10.3847/1538-3881/abd806](https://doi.org/10.3847/1538-3881/abd806)
- Bensby, T., Feltzing, S., & Oey, M. S. 2014, *A&A*, 562, A71, doi: [10.1051/0004-6361/201322631](https://doi.org/10.1051/0004-6361/201322631)
- Blanco-Cuaresma, S. 2019, *MNRAS*, 486, 2075, doi: [10.1093/mnras/stz549](https://doi.org/10.1093/mnras/stz549)
- Blanco-Cuaresma, S., Soubiran, C., Heiter, U., & Jofré, P. 2014, *A&A*, 569, A111, doi: [10.1051/0004-6361/201423945](https://doi.org/10.1051/0004-6361/201423945)
- Boothroyd, A. I., & Sackmann, I. J. 1999, *ApJ*, 510, 232, doi: [10.1086/306546](https://doi.org/10.1086/306546)
- Botelho, R. B., Milone, A. d. C., Meléndez, J., et al. 2020, *MNRAS*, 499, 2196, doi: [10.1093/mnras/staa2917](https://doi.org/10.1093/mnras/staa2917)
- Briley, M. M., Smith, V. V., King, J., & Lambert, D. L. 1997, *AJ*, 113, 306, doi: [10.1086/118253](https://doi.org/10.1086/118253)
- Brooke, J. S. A., Ram, R. S., Western, C. M., et al. 2014, *ApJS*, 210, 23, doi: [10.1088/0067-0049/210/2/23](https://doi.org/10.1088/0067-0049/210/2/23)
- Busso, M., Wasserburg, G. J., Nollert, K. M., & Calandra, A. 2007, *ApJ*, 671, 802, doi: [10.1086/522616](https://doi.org/10.1086/522616)
- Cantiello, M., & Langer, N. 2010, *A&A*, 521, A9, doi: [10.1051/0004-6361/201014305](https://doi.org/10.1051/0004-6361/201014305)
- Cerqui, V., Haywood, M., Di Matteo, P., Katz, D., & Royer, F. 2023, *arXiv e-prints*, arXiv:2306.03126, doi: [10.48550/arXiv.2306.03126](https://doi.org/10.48550/arXiv.2306.03126)
- Chanamé, J., Pinsonneault, M., & Terndrup, D. M. 2005, *ApJ*, 631, 540, doi: [10.1086/432410](https://doi.org/10.1086/432410)
- Charbonnel, C. 1995, *ApJL*, 453, L41, doi: [10.1086/309744](https://doi.org/10.1086/309744)
- Charbonnel, C., & Lagarde, N. 2010, *A&A*, 522, A10, doi: [10.1051/0004-6361/201014432](https://doi.org/10.1051/0004-6361/201014432)
- Charbonnel, C., & Zahn, J. P. 2007, *A&A*, 467, L15, doi: [10.1051/0004-6361:20077274](https://doi.org/10.1051/0004-6361:20077274)
- Chiappini, C., Anders, F., Rodrigues, T. S., et al. 2015, *A&A*, 576, L12, doi: [10.1051/0004-6361/201525865](https://doi.org/10.1051/0004-6361/201525865)
- Denissenkov, P. A., & Tout, C. A. 2000, *MNRAS*, 316, 395, doi: [10.1046/j.1365-8711.2000.03498.x](https://doi.org/10.1046/j.1365-8711.2000.03498.x)
- Eggleton, P. P., Dearborn, D. S. P., & Lattanzio, J. C. 2008, *ApJ*, 677, 581, doi: [10.1086/529024](https://doi.org/10.1086/529024)
- Gaia Collaboration, Brown, A. G. A., Vallenari, A., et al. 2021, *A&A*, 649, A1, doi: [10.1051/0004-6361/202039657](https://doi.org/10.1051/0004-6361/202039657)
- Gaia Collaboration, Vallenari, A., Brown, A. G. A., et al. 2023, *A&A*, 674, A1, doi: [10.1051/0004-6361/202243940](https://doi.org/10.1051/0004-6361/202243940)
- Gerber, J. M., Magg, E., Plez, B., et al. 2023, *A&A*, 669, A43, doi: [10.1051/0004-6361/202243673](https://doi.org/10.1051/0004-6361/202243673)
- Gratton, R. G., Sneden, C., Carretta, E., & Bragaglia, A. 2000, *A&A*, 354, 169
- Green, G. M., Schlafly, E., Zucker, C., Speagle, J. S., & Finkbeiner, D. 2019, *ApJ*, 887, 93, doi: [10.3847/1538-4357/ab5362](https://doi.org/10.3847/1538-4357/ab5362)
- Gustafsson, B., Edvardsson, B., Eriksson, K., et al. 2008, *A&A*, 486, 951, doi: [10.1051/0004-6361:200809724](https://doi.org/10.1051/0004-6361:200809724)
- Harris, C. R., Millman, K. J., van der Walt, S. J., et al. 2020, *Nature*, 585, 357–362, doi: [10.1038/s41586-020-2649-2](https://doi.org/10.1038/s41586-020-2649-2)
- Heiter, U., Lind, K., Bergemann, M., et al. 2021, *A&A*, 645, A106, doi: [10.1051/0004-6361/201936291](https://doi.org/10.1051/0004-6361/201936291)
- Hekker, S., & Johnson, J. A. 2019, *MNRAS*, 487, 4343, doi: [10.1093/mnras/stz1554](https://doi.org/10.1093/mnras/stz1554)
- Hekker, S., & Meléndez, J. 2007, *A&A*, 475, 1003, doi: [10.1051/0004-6361:20078233](https://doi.org/10.1051/0004-6361:20078233)
- Ho, A. Y. Q., Ness, M. K., Hogg, D. W., et al. 2017, *ApJ*, 836, 5, doi: [10.3847/1538-4357/836/1/5](https://doi.org/10.3847/1538-4357/836/1/5)
- Huang, Y., Liu, X.-W., Zhang, H.-W., et al. 2015, *Research in Astronomy and Astrophysics*, 15, 1240, doi: [10.1088/1674-4527/15/8/010](https://doi.org/10.1088/1674-4527/15/8/010)
- Huang, Y., Schönrich, R., Zhang, H., et al. 2020, *ApJS*, 249, 29, doi: [10.3847/1538-4365/ab994f](https://doi.org/10.3847/1538-4365/ab994f)
- Hunter, J. D. 2007, *Computing in Science and Engineering*, 9, 90, doi: [10.1109/MCSE.2007.55](https://doi.org/10.1109/MCSE.2007.55)
- Iben, Icko, J. 1965, *ApJ*, 141, 993, doi: [10.1086/148193](https://doi.org/10.1086/148193)
- Iben, Icko, J. 1967, *ApJ*, 147, 624, doi: [10.1086/149040](https://doi.org/10.1086/149040)
- Izzard, R. G., Preece, H., Jofre, P., et al. 2018, *MNRAS*, 473, 2984, doi: [10.1093/mnras/stx2355](https://doi.org/10.1093/mnras/stx2355)
- Ji, W., Cui, W., Liu, C., et al. 2016, *ApJS*, 226, 1, doi: [10.3847/0067-0049/226/1/1](https://doi.org/10.3847/0067-0049/226/1/1)
- Jofré, P., Jorissen, A., Van Eck, S., et al. 2016, *A&A*, 595, A60, doi: [10.1051/0004-6361/201629356](https://doi.org/10.1051/0004-6361/201629356)
- Jofré, P., Jorissen, A., Aguilera-Gómez, C., et al. 2023, *A&A*, 671, A21, doi: [10.1051/0004-6361/202244524](https://doi.org/10.1051/0004-6361/202244524)
- Jönsson, H., Holtzman, J. A., Allende Prieto, C., et al. 2020, *AJ*, 160, 120, doi: [10.3847/1538-3881/aba592](https://doi.org/10.3847/1538-3881/aba592)
- Keller, L. D., Pilachowski, C. A., & Sneden, C. 2001, *AJ*, 122, 2554, doi: [10.1086/323548](https://doi.org/10.1086/323548)

- Kippenhahn, R., Ruschenplatt, G., & Thomas, H. C. 1980, *A&A*, 91, 175
- Lagarde, N., Decressin, T., Charbonnel, C., et al. 2012, *A&A*, 543, A108, doi: [10.1051/0004-6361/201118331](https://doi.org/10.1051/0004-6361/201118331)
- Lagarde, N., Minkevičiūtė, R., Drazdauskas, A., et al. 2024, *A&A*, 684, A70, doi: [10.1051/0004-6361/202348336](https://doi.org/10.1051/0004-6361/202348336)
- Lambert, D. L. 1978, *MNRAS*, 182, 249, doi: [10.1093/mnras/182.2.249](https://doi.org/10.1093/mnras/182.2.249)
- Lindgren, L., Bastian, U., Biermann, M., et al. 2021, *A&A*, 649, A4, doi: [10.1051/0004-6361/202039653](https://doi.org/10.1051/0004-6361/202039653)
- Lu, Y., Colman, I. L., Sayeed, M., et al. 2024, arXiv e-prints, arXiv:2410.02962, doi: [10.48550/arXiv.2410.02962](https://doi.org/10.48550/arXiv.2410.02962)
- Luo, A. L., Zhao, Y.-H., Zhao, G., et al. 2015, *Research in Astronomy and Astrophysics*, 15, 1095, doi: [10.1088/1674-4527/15/8/002](https://doi.org/10.1088/1674-4527/15/8/002)
- Maas, Z. G., Gerber, J. M., Deibel, A., & Pilachowski, C. A. 2019, *ApJ*, 878, 43, doi: [10.3847/1538-4357/ab1eab](https://doi.org/10.3847/1538-4357/ab1eab)
- Maas, Z. G., Hawkins, K., Hinkel, N. R., et al. 2022, *AJ*, 164, 61, doi: [10.3847/1538-3881/ac77f8](https://doi.org/10.3847/1538-3881/ac77f8)
- Maben, S., Campbell, S. W., Kumar, Y. B., Reddy, B. E., & Zhao, G. 2023, *ApJ*, 957, 18, doi: [10.3847/1538-4357/acf611](https://doi.org/10.3847/1538-4357/acf611)
- Magg, E., Bergemann, M., Serenelli, A., et al. 2022, *A&A*, 661, A140, doi: [10.1051/0004-6361/202142971](https://doi.org/10.1051/0004-6361/202142971)
- Martig, M., Rix, H.-W., Silva Aguirre, V., et al. 2015, *MNRAS*, 451, 2230, doi: [10.1093/mnras/stv1071](https://doi.org/10.1093/mnras/stv1071)
- Masseron, T., Merle, T., & Hawkins, K. 2016a, *BACCHUS: Brussels Automatic Code for Characterizing High accuracy Spectra*, Astrophysics Source Code Library, record ascl:1605.004 <http://ascl.net/1605.004>
- Masseron, T., Merle, T., & Hawkins, K. 2016b, *BACCHUS: Brussels Automatic Code for Characterizing High accuracy Spectra*, Astrophysics Source Code Library, record ascl:1605.004 <http://ascl.net/1605.004>
- Matsuno, T., Yong, D., Aoki, W., & Ishigaki, M. N. 2018, *ApJ*, 860, 49, doi: [10.3847/1538-4357/aac019](https://doi.org/10.3847/1538-4357/aac019)
- McCormick, C., Majewski, S. R., Smith, V. V., et al. 2023, *MNRAS*, 524, 4418, doi: [10.1093/mnras/stad2156](https://doi.org/10.1093/mnras/stad2156)
- Mitchell, Walter E., J., & Mohler, O. C. 1965, *ApJ*, 141, 1126, doi: [10.1086/148202](https://doi.org/10.1086/148202)
- Nordhaus, J., Busso, M., Wasserburg, G. J., Blackman, E. G., & Palmerini, S. 2008, *ApJL*, 684, L29, doi: [10.1086/591963](https://doi.org/10.1086/591963)
- Palacios, A., Charbonnel, C., Talon, S., & Siess, L. 2006, *A&A*, 453, 261, doi: [10.1051/0004-6361:20053065](https://doi.org/10.1051/0004-6361:20053065)
- Palmerini, S., Busso, M., Maiorca, E., & Guandalini, R. 2009, *PASA*, 26, 161, doi: [10.1071/AS08040](https://doi.org/10.1071/AS08040)
- Pinsonneault, M. H., Elsworth, Y., Epstein, C., et al. 2014, *ApJS*, 215, 19, doi: [10.1088/0067-0049/215/2/19](https://doi.org/10.1088/0067-0049/215/2/19)
- Pinsonneault, M. H., Elsworth, Y. P., Tayar, J., et al. 2018, *ApJS*, 239, 32, doi: [10.3847/1538-4365/aabefd](https://doi.org/10.3847/1538-4365/aabefd)
- Plez, B. 2012, *Turbospectrum: Code for spectral synthesis*, Astrophysics Source Code Library, record ascl:1205.004 <http://ascl.net/1205.004>
- Price-Whelan, A. 2018, *adrn/pyia: v0.2, v0.2 Zenodo*, doi: [10.5281/zenodo.1228136](https://doi.org/10.5281/zenodo.1228136)
- Ramírez, I., Allende Prieto, C., & Lambert, D. L. 2013, *ApJ*, 764, 78, doi: [10.1088/0004-637X/764/1/78](https://doi.org/10.1088/0004-637X/764/1/78)
- Recio-Blanco, A., & de Laverny, P. 2007, *A&A*, 461, L13, doi: [10.1051/0004-6361:20066552](https://doi.org/10.1051/0004-6361:20066552)
- Rui, N. Z., & Fuller, J. 2021, *MNRAS*, 508, 1618, doi: [10.1093/mnras/stab2528](https://doi.org/10.1093/mnras/stab2528)
- Schölkopf, B., Smola, A., & Müller, K.-R. 1998, *Neural Computation*, 10, 1299, doi: [10.1162/089976698300017467](https://doi.org/10.1162/089976698300017467)
- Science Software Branch at STScI. 2012, *PyRAF: Python alternative for IRAF*, Astrophysics Source Code Library, record ascl:1207.011 <http://ascl.net/1207.011>
- Shejeelammal, J., Goswami, A., & Shi, J. 2021, *MNRAS*, 502, 1008, doi: [10.1093/mnras/staa3892](https://doi.org/10.1093/mnras/staa3892)
- Shetrone, M. D. 2003, *ApJL*, 585, L45, doi: [10.1086/374262](https://doi.org/10.1086/374262)
- Silva Aguirre, V., Bojsen-Hansen, M., Slumstrup, D., et al. 2018, *MNRAS*, 475, 5487, doi: [10.1093/mnras/sty150](https://doi.org/10.1093/mnras/sty150)
- Smiljanic, R., Gauderon, R., North, P., et al. 2009, *A&A*, 502, 267, doi: [10.1051/0004-6361/200811113](https://doi.org/10.1051/0004-6361/200811113)
- Smith, G. H., Shetrone, M. D., & Strader, J. 2007, *PASP*, 119, 722, doi: [10.1086/521035](https://doi.org/10.1086/521035)
- Smith, V. V., & Lambert, D. L. 1990, *ApJS*, 72, 387, doi: [10.1086/191421](https://doi.org/10.1086/191421)
- Spite, M., Cayrel, R., Hill, V., et al. 2006, *A&A*, 455, 291, doi: [10.1051/0004-6361:20065209](https://doi.org/10.1051/0004-6361:20065209)
- Storm, N., & Bergemann, M. 2023, *MNRAS*, 525, 3718, doi: [10.1093/mnras/stad2488](https://doi.org/10.1093/mnras/stad2488)
- Sun, W. X., Huang, Y., Wang, H. F., et al. 2020, *ApJ*, 903, 12, doi: [10.3847/1538-4357/abb1b7](https://doi.org/10.3847/1538-4357/abb1b7)
- Suntzeff, N. B., & Smith, V. V. 1991, *ApJ*, 381, 160, doi: [10.1086/170638](https://doi.org/10.1086/170638)
- Sweigart, A. V., & Mengel, J. G. 1979, *ApJ*, 229, 624, doi: [10.1086/156996](https://doi.org/10.1086/156996)
- Szigeti, L., Mészáros, S., Smith, V. V., et al. 2018, *MNRAS*, 474, 4810, doi: [10.1093/mnras/stx3027](https://doi.org/10.1093/mnras/stx3027)
- Tautvaišienė, G., Barisevičius, G., Chorniy, Y., Ilyin, I., & Puzeras, E. 2013, *MNRAS*, 430, 621, doi: [10.1093/mnras/sts663](https://doi.org/10.1093/mnras/sts663)
- Tautvaišienė, G., Drazdauskas, A., Bragaglia, A., Randich, S., & Ženovienė, R. 2016, *A&A*, 595, A16, doi: [10.1051/0004-6361/201629273](https://doi.org/10.1051/0004-6361/201629273)

- Tody, D. 1986, in Society of Photo-Optical Instrumentation Engineers (SPIE) Conference Series, Vol. 627, Instrumentation in astronomy VI, ed. D. L. Crawford, 733, doi: [10.1117/12.968154](https://doi.org/10.1117/12.968154)
- Tody, D. 1993, in Astronomical Society of the Pacific Conference Series, Vol. 52, Astronomical Data Analysis Software and Systems II, ed. R. J. Hanisch, R. J. V. Brissenden, & J. Barnes, 173
- Virtanen, P., Gommers, R., Oliphant, T. E., et al. 2020, Nature Methods, 17, 261, doi: [10.1038/s41592-019-0686-2](https://doi.org/10.1038/s41592-019-0686-2)
- Wachlin, F. C., Miller Bertolami, M. M., & Althaus, L. G. 2011, A&A, 533, A139, doi: [10.1051/0004-6361/201117029](https://doi.org/10.1051/0004-6361/201117029)
- Wang, L., Liu, Y., Zhao, G., & Sato, B. 2011, PASJ, 63, 1035, doi: [10.1093/pasj/63.5.1035](https://doi.org/10.1093/pasj/63.5.1035)
- Wang, S., & Chen, X. 2019, ApJ, 877, 116, doi: [10.3847/1538-4357/ab1c61](https://doi.org/10.3847/1538-4357/ab1c61)
- Wu, Y., Xiang, M., Bi, S., et al. 2018, MNRAS, 475, 3633, doi: [10.1093/mnras/stx3296](https://doi.org/10.1093/mnras/stx3296)
- Wu, Y., Xiang, M., Zhao, G., et al. 2019, MNRAS, 484, 5315, doi: [10.1093/mnras/stz256](https://doi.org/10.1093/mnras/stz256)
- Xiang, M. S., Liu, X. W., Yuan, H. B., et al. 2015, MNRAS, 448, 822, doi: [10.1093/mnras/stu2692](https://doi.org/10.1093/mnras/stu2692)
- Xiang, M. S., Liu, X. W., Shi, J. R., et al. 2017, MNRAS, 464, 3657, doi: [10.1093/mnras/stw2523](https://doi.org/10.1093/mnras/stw2523)
- Yong, D., Casagrande, L., Venn, K. A., et al. 2016, MNRAS, 459, 487, doi: [10.1093/mnras/stw676](https://doi.org/10.1093/mnras/stw676)
- Yu, J., Huber, D., Bedding, T. R., et al. 2018, ApJS, 236, 42, doi: [10.3847/1538-4365/aaaf74](https://doi.org/10.3847/1538-4365/aaaf74)
- Zhang, M., Xiang, M., Zhang, H.-W., et al. 2021, ApJ, 922, 145, doi: [10.3847/1538-4357/ac22a5](https://doi.org/10.3847/1538-4357/ac22a5)
- Zhang, X., Jeffery, C. S., Li, Y., & Bi, S. 2020, ApJ, 889, 33, doi: [10.3847/1538-4357/ab5e89](https://doi.org/10.3847/1538-4357/ab5e89)